The Journal of Chemical Physics ARTICLE pubs.aip.org/aip/jcp

General framework for quantifying dissipation pathways in open quantum systems. III. Off-diagonal subsystem–bath couplings

Cite as: J. Chem. Phys. 164, 034105 (2026); doi: 10.1063/5.0305296
Submitted: 5 October 2025 • Accepted: 11 December 2025 •
Published Online: 15 January 2026

Ignacio Gustin,[1] Chang Woo Kim,[2,3,a)] and Ignacio Franco[1,4,5,b)]

AFFILIATIONS

[1] Department of Chemistry, University of Rochester, Rochester, New York 14627, USA
[2] Department of Chemistry, Chonnam National University, Gwangju 61186, South Korea
[3] The Research Institute for Molecular Science, Chonnam National University, Gwangju 61186, South Korea
[4] Department of Physics, University of Rochester, Rochester, New York 14627, USA
[5] Institute of Optics, University of Rochester, Rochester, New York 14627, USA

Note: This paper is part of the Special Topic Festschrift in honor of Jianshu Cao: Non-Equilibrium Kinetics and Quantum Dynamics.

[a)] **Author to whom correspondence should be addressed:** cwkim66@chonnam.ac.kr
[b)] **Electronic mail:** ignacio.franco@rochester.edu

ABSTRACT

This paper extends the previously reported theory of dissipation pathways [C. W. Kim and I. Franco, J. Chem. Phys. **160**, 214111 (2024)] to incorporate off-diagonal subsystem–bath coupling, which is often required to model molecular systems where the environment directly influences transitions and couplings between subsystem states. We systematically derive master equations for both population transfer and dissipation into individual bath components, for which we also rigorously prove energy conservation and detailed balance. The approach is based on second-order perturbation theory with respect to the subsystem–bath couplings, whose form is not limited to any specific model. The accuracy of the developed method is tested by applying it to diverse model Hamiltonians involving linearly coupled harmonic oscillator baths and comparing the outcomes against the hierarchical equations of motion (HEOM) method. Overall, our method accurately quantifies the contributions of specific bath components to the overall dissipation while significantly reducing the computational cost compared to numerically exact methods such as HEOM, thus offering a path to examine how vibronic interactions steer non-adiabatic processes in realistic chemical systems.

I. INTRODUCTION

A wide range of quantum chemical phenomena are non-equilibrium processes where the excess energy is dissipated from the central subsystem to the surrounding environment. Naturally, examining this energy flow in detail can provide fundamental insights to understand chemical reactions, material properties, and essential biological processes. For instance, elucidating the major dissipation pathways is crucial for grasping how photosynthetic complexes transfer energy[1–3] and designing physical systems that enhance or suppress dissipation.[4–8]

While the basic principles of energy transfer are well-established, elucidating the precise pathways of energy flow remains challenging, as it amounts to resolving the energy transport within complex molecular environments at a microscopic level. Addressing this challenge requires a method capable of effectively decomposing the overall dissipation into the contributions of individual environmental components. To accomplish this task, it is necessary to fully capture the dynamical information regarding individual vibronic quantum states, which is often computationally prohibitive even with state-of-the-art simulation methods for quantum dynamics. For example, explicit approaches such as the multi-configurational

time-dependent Hartree (MCTDH)[9] method, which accurately track the dynamics via direct wavefunction propagation, become computationally intractable for macroscopic thermal environments. By contrast, quantum master equations (QMEs) and related techniques[10–13] can cope with complex chemical environments by focusing on their implicit effect on the dynamics within the subsystem. However, this ability comes at the cost of losing information regarding the quantum states of the environment.

To address this challenge, we recently introduced QME-D,[14] a general theoretical framework for quantifying and resolving dissipation pathways in complex quantum systems involving highly structured thermal environments. The theoretical framework utilizes the Nakajima–Zwanzig projection operator technique,[15,16] which is combined with second-order perturbation theory with respect to the coupling between the subsystem states.[14,17] The framework was proven to be useful in unraveling the detailed dissipation pathways in the realistic model of the Fenna–Matthews–Olson photosynthetic complex.[18]

Despite the success of the QME-D in studying the quantum dynamics of molecular systems, its applicability is still limited by the assumption that the bath couples only to the diagonal part of the subsystem Hamiltonian matrix. Under such settings, the bath only modulates the energies of the subsystem states and, therefore, does not directly mediate population transfer. In molecular systems, this is equivalent to the Condon approximation, under which couplings between molecular electronic states are unaffected by the nuclei. However, there are various situations where intramolecular vibrations or solvent can actively modulate the electronic couplings to induce non-adiabatic transitions. These considerations motivate us to generalize the previously reported framework for quantifying dissipation pathways to handle both on- and off-diagonal subsystem–bath coupling. As a result, the bath is allowed to directly mediate transitions between subsystem states, which better describes the dynamics occurring in a broad range of quantum transport processes involving molecules.

The structure of this paper is as follows: In Secs. II A–II C, we provide an overview of the theoretical background required to understand the main findings of our work and introduce the extended framework for quantifying dissipation pathways. Subsequently, Sec. II D applies the newly developed approach to specific model Hamiltonians and connects the outcomes with previously established results. In Sec. III, we extensively test the accuracy of our framework against a numerically exact dissipation calculation based on hierarchical equations of motion (HEOM), while also comparing the performance with QME-D[14,19] to highlight the utility of the new approach. Section IV concludes by summarizing the principal findings and discussing conceivable future research directions.

II. THEORY

A. Population transfer

We take the standard viewpoint for open quantum system dynamics and divide the system Hamiltonian $\hat{H}$ as

$$\hat{H} = \hat{H}_{\mathrm{S}} + \hat{H}_{\mathrm{B}} + \hat{H}_{\mathrm{SB}}, \tag{1}$$

where $\hat{H}_{\mathrm{S}}$, $\hat{H}_{\mathrm{B}}$, and $\hat{H}_{\mathrm{SB}}$ are the Hamiltonian components for the subsystem, the bath, and the subsystem–bath interaction, respectively. The subsystem Hamiltonian $\hat{H}_{\mathrm{S}}$ generally takes the form

$$\hat{H}_{\mathrm{S}} = \sum_A \sum_B H_{AB}|A\rangle\langle B|, \tag{2}$$

where uppercase Roman alphabets are used to label the individual subsystem states, which will be referred to as the diabatic basis throughout the rest of this paper. The elements of $\hat{H}_{\mathrm{S}}$ satisfy $H_{AB} = H_{BA}^*$ due to the Hermicity.

Having specified the subsystem, we assume that the rest of the Hamiltonian can be split into contributions from independent bath components. This is formally expressed as

$$\hat{H}_{\mathrm{B}} + \hat{H}_{\mathrm{SB}} = \sum_j \hat{h}_j, \tag{3}$$

where $\{\hat{h}_j\}$ arises from the jth bath component and can take a general form of

$$\hat{h}_j = \sum_A \sum_B (|A\rangle\langle B| \otimes \hat{v}_{AB}^j). \tag{4}$$

The Hermicity requires that the operators in the bath subspace satisfy $\hat{v}_{AB}^j = (\hat{v}_{AB}^j)^\dagger$. The individual bath components only interact through the subsystem and do not directly affect each other, establishing the commutativity between operators with different j's. We note that Eq. (4) is in contrast to the work presented in Ref. 14, where we only allowed the bath to couple to the subsystem through the diagonal component of $\hat{H}_{\mathrm{S}}$.

We now diagonalize $\hat{H}_{\mathrm{S}}$ and compute its eigenenergies and eigenstates,

$$\hat{H}_{\mathrm{S}} = \sum_\alpha E_\alpha|\alpha\rangle\langle\alpha|, \tag{5}$$

where each eigenstate $|\alpha\rangle$ is a linear superposition of the diabatic states,

$$|\alpha\rangle = \sum_\alpha c_{\alpha A}|A\rangle. \tag{6}$$

The basis $\{|\alpha\rangle\}$ is often called the exciton basis and will be labeled with the Greek alphabet from now on. Recasting Eq. (4) using Eq. (6) yields

$$\hat{h}_j = \sum_{\alpha,\beta} (|\alpha\rangle\langle\beta| \otimes \hat{v}_{\alpha\beta}^j), \tag{7}$$

where the bath-related operators are transformed as

$$\hat{v}_{\alpha\beta}^j = \sum_A \sum_B c_{\alpha A}^* c_{\beta B} \hat{v}_{AB}^j. \tag{8}$$

It should be noted that there is a freedom of choice for the boundary between the subsystem and the bath, on which the elements of $\hat{H}_{\mathrm{S}}$ [Eq. (2)] depend. Hence, the exciton basis $\{|\alpha\rangle\}$ and the transformation coefficients $\{c_{\alpha A}\}$ are not uniquely determined. We will revisit this point in Sec. II D, where we apply our theory to specific model systems.

The density operator $\hat{\rho}$ for the system evolves according to the Liouville–von Neumann equation $d\hat{\rho}(t)/dt = -i\mathscr{L}\hat{\rho}(t)/\hbar$, where

$\mathscr{L}$ is the Liouvillian super-operator whose action is defined as $\mathscr{L}\hat{O} = [\hat{H}, \hat{O}]$ for an arbitrary operator $\hat{O}$. We apply the perturbation theory in the exciton basis by dividing $\hat{H}$ into the diagonal component $\hat{H}_0$ and off-diagonal component $\hat{H}_1$, namely,

$$\hat{H}_0 = \sum_\alpha [|\alpha\rangle\langle\alpha| \otimes (E_\alpha + \hat{V}_{\alpha\alpha})], \tag{9a}$$

$$\hat{H}_1 = \sum_\alpha \sum_{\beta\neq\alpha} (|\alpha\rangle\langle\beta| \otimes \hat{V}_{\alpha\beta}) + \text{H.c.}, \tag{9b}$$

and treat $\hat{H}_1$ as the perturbation. In the above, H.c. is the abbreviation for the Hermitian conjugate, and the collective bath operators $\{\hat{V}_{\alpha\beta}\}$ are defined as

$$\hat{V}_{\alpha\beta} = \langle\alpha|\hat{H}_\text{B} + \hat{H}_\text{SB}|\beta\rangle = \sum_j \hat{v}^j_{\alpha\beta}. \tag{10}$$

The Liouvillian is also accordingly divided into $\mathscr{L} = \mathscr{L}_0 + \mathscr{L}_1$, where $\mathscr{L}_0\hat{O} = [\hat{H}_0, \hat{O}]$ and $\mathscr{L}_1\hat{O} = [\hat{H}_1, \hat{O}]$.

We now apply the projection operator technique[15,16] to derive the quantum master equation for the evolution of $\hat{\rho}(t)$. We begin by splitting the identity super-operator in the Liouville space into $\mathscr{I} = \mathscr{P} + \mathscr{Q}$, where $\mathscr{P}$ and $\mathscr{Q}$ project $\hat{\rho}$ onto the dynamically relevant part $\mathscr{P}\hat{\rho}$ and the remaining $\mathscr{Q}\hat{\rho}$, respectively. Because $\mathscr{P}$ and $\mathscr{Q}$ are projection operators, they should satisfy $\mathscr{P}^2 = \mathscr{P}$ and also $\mathscr{P}\mathscr{Q} = \mathscr{Q}\mathscr{P} = 0$. At this point, we specify the form of $\mathscr{P}$ as

$$\mathscr{P}\hat{\rho} = \sum_\alpha P_\alpha|\alpha\rangle\langle\alpha| \otimes \hat{R}_\alpha, \tag{11}$$

where $P_\alpha = \text{Tr}_\text{b}\langle\alpha|\hat{\rho}|\alpha\rangle$ is the population of the state $|\alpha\rangle$, Tr_b indicates the trace over the bath, and $\hat{R}_\alpha$ is the equilibrium bath density associated with $\hat{V}_{\alpha\alpha}$,

$$\hat{R}_\alpha = \frac{\exp(-\beta\hat{V}_{\alpha\alpha})}{\text{Tr}_\text{b}[\exp(-\beta\hat{V}_{\alpha\alpha})]}. \tag{12}$$

The inverse temperature $\beta = 1/k_\text{B}T$ should not be confused with the exciton index β, which is only used as a subscript.

At the initial time, we assume that the system density is confined in the dynamically relevant part, that is, $\mathscr{P}\hat{\rho}(0) = \hat{\rho}(0)$ and $\mathscr{Q}\hat{\rho}(0) = 0$. The evolution of $\mathscr{P}\hat{\rho}(t)$ under second-order perturbation theory follows,[14,20,21]

$$\frac{d}{dt}[\mathscr{P}\hat{\rho}(t)] \approx -\frac{1}{\hbar^2}\int_0^t \mathscr{P}\mathscr{L}_1 \exp\left[-\frac{i(t-\tau)}{\hbar}\mathscr{L}_0\right]\mathscr{L}_1\mathscr{P}\hat{\rho}(\tau)\,d\tau, \tag{13}$$

to which we make a substitution $t - \tau = t'$ and apply Markov approximation by replacing $\hat{\rho}(t - t')$ with $\hat{\rho}(t)$ and extending the upper limit of the integration to infinity. After calculating $\text{Tr}_\text{b}[\langle\alpha|\frac{d}{dt}\{\mathscr{P}\hat{\rho}(t)\}|\alpha\rangle]$ from the resulting expression, we obtain a time-local equation-of-motion for the exciton populations,

$$\dot{P}_\alpha(t) = -\frac{1}{\hbar^2}\text{Tr}_\text{b}\left[\int_0^\infty \langle\alpha|\mathscr{P}\mathscr{L}_1 \exp(-it'\mathscr{L}_0/\hbar)\mathscr{L}_1\mathscr{P}\hat{\rho}(t)|\alpha\rangle\,dt'\right]. \tag{14}$$

Expanding the exponential in Eq. (14) leads to a first-order rate equation,

$$\dot{P}_\alpha(t) = \sum_{\beta\neq\alpha}[-K_{\beta\alpha}P_\alpha(t) + K_{\alpha\beta}P_\beta(t)], \tag{15}$$

where the rate constants are expressed as

$$K_{\beta\alpha} = \frac{2}{\hbar^2}\,\text{Re}\int_0^\infty \exp\left(\frac{-it'(E_\beta - E_\alpha)}{\hbar}\right)S_{\beta\alpha}(t')\,dt', \tag{16}$$

$$S_{\beta\alpha}(t') = \text{Tr}_\text{b}\left[\hat{U}^\dagger_\alpha(t')\hat{V}_{\alpha\beta}\hat{U}_\beta(t')\hat{V}_{\beta\alpha}\hat{R}_\alpha\right], \tag{17}$$

with the time-dependent unitary operators $\{\hat{U}_\alpha(t')\}$ defined by

$$\hat{U}_\alpha(t') = \exp\left(-\frac{it'\hat{V}_{\alpha\alpha}}{\hbar}\right). \tag{18}$$

The condition that the integral in Eq. (16) is well-defined,

$$\lim_{t'\to\infty} S_{\beta\alpha}(t') = 0, \tag{19}$$

will play a crucial role in the proof of energy conservation in Sec. II C 1. Integrating Eq. (16) requires us to accurately determine $S_{\beta\alpha}(t')$ up to an arbitrary time point. For this, we factorize the unitary operator [Eq. (18)] and equilibrium bath density [Eq. (12)] into contributions from individual bath components,

$$\hat{U}_\alpha(t') = \prod_j \hat{u}^j_\alpha(t'), \quad \hat{u}^j_\alpha(t') = \exp\left(-\frac{it'\hat{v}^j_{\alpha\alpha}}{\hbar}\right) \tag{20}$$

and

$$\hat{R}_\alpha = \prod_j \hat{r}^j_\alpha, \quad \hat{r}^j_\alpha = \frac{\exp(-\beta\hat{v}^j_{\alpha\alpha})}{\text{Tr}_j[\exp(-\beta\hat{v}^j_{\alpha\alpha})]}. \tag{21}$$

Here, Tr_j indicates the trace over the subspace spanned by the jth bath component. For succinctness, the dependence on t' of the scalars and operators will be omitted hereafter, unless required for clarity.

We now define the abbreviation for the traces,

$$\text{Tr0}^j_{\beta\alpha} \equiv \text{Tr}_j\left[(\hat{u}^j_\alpha)^\dagger\hat{u}^j_\beta\hat{r}^j_\alpha\right], \tag{22a}$$

$$\text{Tr1}^j_{\beta\alpha} \equiv \text{Tr}_j\left[(\hat{u}^j_\alpha)^\dagger\hat{v}^j_{\alpha\beta}\hat{u}^j_\beta\hat{r}^j_\alpha\right], \tag{22b}$$

$$\text{Tr2}^j_{\beta\alpha} \equiv \text{Tr}_j\left[(\hat{u}^j_\alpha)^\dagger\hat{u}^j_\beta\hat{v}^j_{\beta\alpha}\hat{r}^j_\alpha\right], \tag{22c}$$

$$\text{Tr3}^j_{\beta\alpha} \equiv \text{Tr}_j\left[(\hat{u}^j_\alpha)^\dagger\hat{v}^j_{\alpha\beta}\hat{u}^j_\beta\hat{v}^j_{\beta\alpha}\hat{r}^j_\alpha\right]. \tag{22d}$$

By adopting this notation, the trace in Eq. (17) can be expressed as

$$S_{\beta\alpha}(t') = \sum_j\left[\text{Tr3}^j_{\beta\alpha}\prod_{k\neq j}\text{Tr0}^k_{\beta\alpha} + \sum_{k\neq j}\left(\text{Tr1}^j_{\beta\alpha}\text{Tr2}^k_{\beta\alpha}\prod_{l\neq(j,k)}\text{Tr0}^l_{\beta\alpha}\right)\right]. \tag{23}$$

Because we did not adopt any specific model of the bath up to this point, Eq. (23) is valid for arbitrary bath and subsystem–bath interaction, as long as they can be decomposed into the form of Eq. (3). Importantly, Eq. (23) disentangles the trace for the full bath subspace [Eq. (17)] into the traces for individual bath components [Eq. (22)]. To numerically evaluate Eq. (22) for all bath components, we can convert Eq. (23) to a more practical expression by defining

$$W_{\beta\alpha} \equiv \sum_j \frac{\mathrm{Tr}1^j_{\beta\alpha}}{\mathrm{Tr}0^j_{\beta\alpha}}, \quad X_{\beta\alpha} \equiv \sum_j \frac{\mathrm{Tr}2^j_{\beta\alpha}}{\mathrm{Tr}0^j_{\beta\alpha}},$$
$$Y_{\beta\alpha} \equiv \sum_j \frac{\mathrm{Tr}3^j_{\beta\alpha}}{\mathrm{Tr}0^j_{\beta\alpha}}, \quad \Pi_{\beta\alpha} \equiv \prod_j \mathrm{Tr}0^j_{\beta\alpha}, \tag{24}$$
$$Z_{\beta\alpha} \equiv \sum_j \frac{\mathrm{Tr}1^j_{\beta\alpha}\,\mathrm{Tr}2^j_{\beta\alpha}}{(\mathrm{Tr}0^j_{\beta\alpha})^2},$$

such that

$$S_{\beta\alpha}(t') = (W_{\beta\alpha}X_{\beta\alpha} + Y_{\beta\alpha} - Z_{\beta\alpha})\Pi_{\beta\alpha}. \tag{25}$$

Equations (24) and (25) evaluate $S_{\beta\alpha}(t')$ at a computational cost proportional to $\mathcal{O}(n)$, instead of the naïve implementation of Eq. (23), which scales as $\mathcal{O}(n^2)$ due to the existence of the double summation.

As we will demonstrate in Sec. II D 1, for relatively simple bath models such as harmonic oscillators with linear subsystem–bath coupling, it is even possible to condense Eq. (25) into a single analytical expression. However, there may also be situations where this simplification is not feasible. In such cases, we can utilize an incremental formula,

$$S_{\beta\alpha}(t') = \left[\mathrm{Tr}3^j_{\beta\alpha} + (\mathrm{Tr}2^j_{\beta\alpha})W^{j-}_{\beta\alpha} + (\mathrm{Tr}1^j_{\beta\alpha})X^{j-}_{\beta\alpha}\right]\Pi^{j-}_{\beta\alpha} + (\mathrm{Tr}0^j_{\beta\alpha})S^{j-}_{\beta\alpha}(t'), \tag{26}$$

where the quantities with the subscript $j-$ are similarly defined as in Eq. (25), but they exclude the contribution from the jth bath component,

$$W^{j-}_{\beta\alpha} \equiv \sum_{k\neq j} \frac{\mathrm{Tr}1^k_{\beta\alpha}}{\mathrm{Tr}0^k_{\beta\alpha}}, \quad X^{j-}_{\beta\alpha} \equiv \sum_{k\neq j} \frac{\mathrm{Tr}2^k_{\beta\alpha}}{\mathrm{Tr}0^k_{\beta\alpha}},$$
$$Y^{j-}_{\beta\alpha} \equiv \sum_{k\neq j} \frac{\mathrm{Tr}3^k_{\beta\alpha}}{\mathrm{Tr}0^k_{\beta\alpha}}, \quad \Pi^{j-}_{\beta\alpha} \equiv \prod_{k\neq j} \mathrm{Tr}0^k_{\beta\alpha}, \tag{27}$$
$$Z^{j-}_{\beta\alpha} \equiv \sum_{k\neq j} \frac{\mathrm{Tr}1^k_{\beta\alpha}\,\mathrm{Tr}2^k_{\beta\alpha}}{(\mathrm{Tr}0^k_{\beta\alpha})^2}.$$

By using Eq. (26), we can efficiently calculate $S_{\beta\alpha}(t')$ by successively incorporating the effect of problematic components into the analytical expression already representing most of the bath, rather than immediately retreating to the direct application of Eqs. (24) and (25).

B. Dissipation

To quantify the dissipation into individual bath components [Eq. (3)], we need to evaluate the rate of dissipation for the jth bath component as[14]

$$\dot{E}_j(t) = \mathrm{Tr}\left[\hat{h}_j \frac{d}{dt}[\mathscr{P}_{j-}\hat{\rho}(t)]\right]. \tag{28}$$

Equation (28) features a new projection operator $\mathscr{P}_{j-}$ that satisfies $\mathscr{P} = \hat{p}_j\mathscr{P}_{j-}$, where

$$\hat{p}_j\hat{\rho} = \sum_\alpha \left(\mathrm{Tr}_j[\langle\alpha|\hat{\rho}|\alpha\rangle]|\alpha\rangle\langle\alpha| \otimes \hat{r}^j_\alpha\right), \tag{29}$$

$$\mathscr{P}_{j-}\hat{\rho} = \sum_\alpha \left(\mathrm{Tr}^{j-}_{\mathrm{b}}[\langle\alpha|\hat{\rho}|\alpha\rangle]|\alpha\rangle\langle\alpha| \otimes \hat{R}^{j-}_\alpha\right). \tag{30}$$

Here, $\mathrm{Tr}^{j-}_{\mathrm{b}}$ denotes the trace over the subspace of all bath components except the jth bath component, and $\hat{R}^{j-}_\alpha$ is the equilibrium bath density in this subspace,

$$\hat{R}^{j-}_\alpha = \prod_{k\neq j} \hat{r}^k_\alpha. \tag{31}$$

Employing $\mathscr{P}_{j-}$ [Eq. (30)] in Eq. (28) removes the projection for the jth bath component, which is crucial for quantifying the dissipation by this component after an infinitesimal amount of time.[14] After calculating the dissipation, the system density returns to the fully projected form $\mathscr{P}\hat{\rho}$ by applying the remaining part of the projection operator $\hat{p}_j$ [Eq. (29)], achieving consistency with the population dynamics governed by Eq. (15).

We aim to develop a practical method for evaluating Eq. (28). We start by observing that the time-evolution of $\mathscr{P}_{j-}\hat{\rho}(t)$ under the second-order perturbation theory follows the equation of motion similar to Eq. (13) except $\mathscr{P}$ is replaced by $\mathscr{P}_{j-}$,[14]

$$\frac{d}{dt}[\mathscr{P}_{j-}\hat{\rho}(t)] = -\frac{1}{\hbar^2}\int_0^t \mathscr{P}_{j-}\mathscr{L}_1 \exp\left[-\frac{i(t-\tau)}{\hbar}\mathscr{L}_0\right] \times \mathscr{L}_1\mathscr{P}_{j-}\hat{\rho}(\tau)\,d\tau. \tag{32}$$

Applying the Markov approximation gives

$$\frac{d}{dt}[\mathscr{P}_{j-}\hat{\rho}(t)] = -\frac{1}{\hbar^2}\int_0^\infty \mathscr{P}_{j-}\mathscr{L}_1 \exp(-it'\mathscr{L}_0/\hbar)\mathscr{L}_1\mathscr{P}_{j-}\hat{\rho}(t)\,dt'. \tag{33}$$

Because we are focusing on the evolution of $\mathscr{P}\hat{\rho}(t)$, it is valid to assume that $\hat{\rho}(t) = \mathscr{P}\hat{\rho}(t)$ is satisfied at every instance. Under this circumstance, the integrand of Eq. (33) can be expanded as

$$\begin{aligned}\mathscr{P}_{j-}\mathscr{L}_1 \exp(-it'\mathscr{L}_0/\hbar)\mathscr{L}_1\mathscr{P}_{j-} &= \sum_\alpha\sum_{\beta\neq\alpha}\left[\exp\left(-\frac{it'(E_\beta - E_\alpha)}{\hbar}\right)|\alpha\rangle\langle\alpha| \otimes \hat{R}^{j-}_\alpha \otimes \left(P_\alpha(t)\mathrm{Tr}^{j-}_{\mathrm{b}}\left[\hat{V}_{\alpha\beta}\hat{U}_\beta\hat{V}_{\beta\alpha}\hat{R}_\alpha\hat{U}^\dagger_\alpha\right] - P_\beta(t)\mathrm{Tr}^{j-}_{\mathrm{b}}\left[\hat{V}_{\alpha\beta}\hat{U}_\beta\hat{R}_\beta\hat{V}_{\beta\alpha}\hat{U}^\dagger_\alpha\right]\right)\right] + \mathrm{H.c.},\end{aligned} \tag{34}$$

where the traces on the right-hand side are now operators related to the jth bath component, rather than scalars as in Eq. (16). We now switch α and β for the two terms involving $P_\beta(t)$ on the right-hand side of Eq. (33), which is justified by the fact that the summation is over all ordered pairs of α and β. The resulting expression can then be used with Eq. (7) to evaluate the right-hand side of Eq. (28), leading to a first-order rate equation for the dissipation,

$$\dot{E}_j(t) = \sum_\alpha\sum_{\beta\neq\alpha} \mathscr{K}^j_{\beta\alpha}P_\alpha(t), \tag{35}$$

with the rate constants given by

$$\mathscr{K}^j_{\beta\alpha} = \frac{2}{\hbar^2}\,\mathrm{Re}\int_0^\infty \exp\left(-\frac{it'(E_\beta - E_\alpha)}{\hbar}\right)\mathscr{J}^j_{\beta\alpha}(t')\,dt', \tag{36}$$

$$\mathscr{S}^{j}_{\beta\alpha}(t') = \mathrm{Tr}_{\mathrm{b}}\left[\hat{v}^{j}_{\beta\beta}\hat{U}_{\beta}\hat{V}_{\beta\alpha}\hat{R}_{\alpha}\hat{U}^{\dagger}_{\alpha}\hat{V}_{\alpha\beta}\right] - \mathrm{Tr}_{\mathrm{b}}\left[\hat{v}^{j}_{\alpha\alpha}\hat{V}_{\alpha\beta}\hat{U}_{\beta}\hat{V}_{\beta\alpha}\hat{R}_{\alpha}\hat{U}^{\dagger}_{\alpha}\right]. \tag{37}$$

As for the population transfer rate constants $\{K_{\beta\alpha}\}$ [Eq. (16)], explicit evaluation of Eq. (36) requires disassembling $\mathscr{S}^{j}_{\beta\alpha}(t')$ [Eq. (37)] into contributions arising from individual bath components. For this purpose, we extend the shorthand notation introduced in Eq. (22) by additionally defining

$$\mathrm{Tr}4^{j}_{\beta\alpha} \equiv \mathrm{Tr}_{j}\left[(\hat{u}^{j}_{\alpha})^{\dagger}(\hat{v}^{j}_{\beta\beta} - \hat{v}^{j}_{\alpha\alpha})\hat{u}^{j}_{\beta}\hat{r}^{j}_{\alpha}\right] = i\hbar\frac{d\,\mathrm{Tr}0^{j}_{\beta\alpha}}{dt'}, \tag{38a}$$

$$\mathrm{Tr}5^{j}_{\beta\alpha} \equiv \mathrm{Tr}_{j}\left[(\hat{u}^{j}_{\alpha})^{\dagger}(\hat{v}^{j}_{\alpha\beta}\hat{v}^{j}_{\beta\beta} - \hat{v}^{j}_{\alpha\alpha}\hat{v}^{j}_{\alpha\beta})\hat{u}^{j}_{\beta}\hat{r}^{j}_{\alpha}\right] = i\hbar\frac{d\,\mathrm{Tr}1^{j}_{\beta\alpha}}{dt'}, \tag{38b}$$

$$\mathrm{Tr}6^{j}_{\beta\alpha} \equiv \mathrm{Tr}\left[(\hat{u}^{j}_{\alpha})^{\dagger}(\hat{v}^{j}_{\beta\beta} - \hat{v}^{j}_{\alpha\alpha})\hat{u}^{j}_{\beta}\hat{v}^{j}_{\beta\alpha}\hat{r}^{j}_{\alpha}\right] = i\hbar\frac{d\,\mathrm{Tr}2^{j}_{\beta\alpha}}{dt'}, \tag{38c}$$

$$\mathrm{Tr}7^{j}_{\beta\alpha} \equiv \mathrm{Tr}_{j}\left[(\hat{u}^{j}_{\alpha})^{\dagger}(\hat{v}^{j}_{\alpha\beta}\hat{v}^{j}_{\beta\beta} - \hat{v}^{j}_{\alpha\alpha}\hat{v}^{j}_{\alpha\beta})\hat{u}^{j}_{\beta}\hat{v}^{j}_{\beta\alpha}\hat{r}^{j}_{\alpha}\right] = i\hbar\frac{d\,\mathrm{Tr}3^{j}_{\beta\alpha}}{dt'}, \tag{38d}$$

and express $\mathscr{S}^{j}_{\beta\alpha}(t')$ in terms of the traces for individual bath components [Eqs. (22) and (38)]. The resulting expression can be simplified using the abbreviated notation in Eq. (24),

$$\mathscr{S}^{j}_{\beta\alpha}(t') = \left[(\mathrm{Tr}6^{j}_{\beta\alpha})W^{j-}_{\beta\alpha} + (\mathrm{Tr}5^{j}_{\beta\alpha})X^{j-}_{\beta\alpha}\right]\Pi^{j-}_{\beta\alpha} + \mathrm{Tr}7^{j}_{\beta\alpha} + (\mathrm{Tr}4^{j}_{\beta\alpha})S^{j-}_{\beta\alpha}(t'). \tag{39}$$

C. Proof of thermodynamic principles

1. Energy conservation

To prove energy conservation, we need to show that the rate of energy loss from the subsystem is equal to the rate of energy gain by the bath,

$$\frac{d}{dt}\mathrm{Tr}\left[\hat{H}_{\mathrm{S}}\mathscr{P}\hat{\rho}(t)\right] + \sum_{j}\dot{E}_{j}(t) \stackrel{?}{=} 0, \tag{40}$$

within our scope, which focuses on $\mathscr{P}\hat{\rho}(t)$.

We eliminate the time-derivatives in Eq. (40) by invoking Eqs. (5), (11), (15), and (35), and then rearrange the resulting expression to get

$$\sum_{\alpha}\sum_{\beta\neq\alpha}\left((E_{\beta} - E_{\alpha})K_{\beta\alpha} + \sum_{j}\mathscr{K}^{j}_{\beta\alpha}\right)P_{\alpha}(t) \stackrel{?}{=} 0. \tag{41}$$

The requirement for Eq. (41) to be satisfied for an arbitrary set of populations $\{P_{\alpha}(t)\}$ is

$$(E_{\beta} - E_{\alpha})K_{\beta\alpha} + \sum_{j}\mathscr{K}^{j}_{\beta\alpha} \stackrel{?}{=} 0, \tag{42}$$

for any pair of α and β. Replacing the population transfer and dissipation rate constants with their explicit expressions [Eqs. (16), (17), (36), and (37)] gives

$$\begin{aligned}(E_{\beta} - E_{\alpha})K_{\beta\alpha} + \sum_{j}\mathscr{K}^{j}_{\beta\alpha} &= \frac{2}{\hbar^{2}}\,\mathrm{Re}\int_{0}^{\infty}\times\left(\mathrm{Tr}_{\mathrm{b}}\left[(E_{\beta} + \hat{V}_{\beta\beta})\hat{U}_{\beta}\hat{V}_{\beta\alpha}\hat{R}_{\alpha}\hat{U}^{\dagger}_{\alpha}\hat{V}_{\alpha\beta}\right]\right.\\ &\left. - \mathrm{Tr}_{\mathrm{b}}\left[(E_{\alpha} + \hat{V}_{\alpha\alpha})\hat{V}_{\alpha\beta}\hat{U}_{\beta}\hat{V}_{\beta\alpha}\hat{R}_{\alpha}\hat{U}^{\dagger}_{\alpha}\right]\right)\\ &\times\exp\left(-\frac{it'(E_{\beta} - E_{\alpha})}{\hbar}\right)dt',\end{aligned} \tag{43}$$

where we used Eq. (10) to condense the sum of the operators for individual bath components. Then, we invoke Eqs. (17) and (18) to express the integrand on the right-hand side of Eq. (43) as a time-derivative,

$$(E_{\beta} - E_{\alpha})K_{\beta\alpha} + \sum_{j}\mathscr{K}^{j}_{\beta\alpha} = \frac{2}{\hbar^{2}}\,\mathrm{Re}\int_{0}^{\infty}i\hbar\frac{d}{dt'}\exp\left(-\frac{it'(E_{\beta} - E_{\alpha})}{\hbar}\right)\times S_{\beta\alpha}(t')\,dt'. \tag{44}$$

We can now carry out the integration and simplify the result with $\hat{U}_{\alpha}(0) = 1$ and Eq. (19) to obtain

$$\int_{0}^{\infty}\left(i\hbar\frac{d}{dt'}\mathrm{Tr}_{\mathrm{b}}\left[\hat{U}^{\dagger}_{\alpha}\hat{V}_{\alpha\beta}\hat{U}_{\beta}\hat{V}_{\beta\alpha}\hat{R}_{\alpha}\right]\right)dt' = i\hbar\,\mathrm{Tr}_{\mathrm{b}}\left[\hat{V}_{\alpha\beta}\hat{V}_{\beta\alpha}\hat{R}_{\alpha}\right], \tag{45}$$

whose value is purely imaginary as $\mathrm{Tr}_{\mathrm{b}}[\hat{V}_{\alpha\beta}\hat{V}_{\beta\alpha}\hat{R}_{\alpha}] = \mathrm{Tr}_{\mathrm{b}}[(\hat{V}_{\alpha\beta}\hat{V}_{\beta\alpha}\hat{R}_{\alpha})^{\dagger}]$ is real. As a result, the right-hand side of Eq. (44) vanishes and assures the validity of Eq. (41) and, in turn, Eq. (40). Therefore, we can conclude that the dissipation calculated by Eqs. (35)–(37) satisfies the energy conservation and achieves consistency with the population dynamics.

2. Detailed balance

For the dynamics of population and dissipation governed by Eqs. (15) and (35), the detailed balance condition is represented as

$$-\frac{\mathscr{K}^{j}_{\alpha\beta}}{\mathscr{K}^{j}_{\beta\alpha}} = \frac{K_{\alpha\beta}}{K_{\beta\alpha}} = \frac{P_{\alpha}(\infty)}{P_{\beta}(\infty)}, \tag{46}$$

which makes the net dissipation by any bath component vanish at the steady state. To prove Eq. (46), we start by applying the Wick rotation $t' \to t' - i\hbar\beta$ to $S_{\beta\alpha}(t')$ [Eq. (17)],

$$S_{\beta\alpha}(t' - i\hbar\beta) = \mathrm{Tr}_{\mathrm{b}}\left[\exp(\beta\hat{V}_{\alpha\alpha})\hat{U}^{\dagger}_{\alpha}\hat{V}_{\alpha\beta}\hat{U}_{\beta}\exp(-\beta\hat{V}_{\beta\beta})\hat{V}_{\beta\alpha}\hat{R}_{\alpha}\right], \tag{47}$$

and rearrange the right-hand side to get

$$S_{\beta\alpha}(t' - i\hbar\beta) = \frac{\mathrm{Tr}_{\mathrm{b}}[\exp(-\beta\hat{V}_{\beta\beta})]}{\mathrm{Tr}_{\mathrm{b}}[\exp(-\beta\hat{V}_{\alpha\alpha})]}\left[S_{\alpha\beta}(t')\right]^{*}, \tag{48}$$

which can be readily validated by using the cyclic invariance of the trace and the definition of the thermal bath density [Eq. (12)]. If we define the Fourier transform of $S_{\beta\alpha}(t')$ as $\tilde{S}_{\beta\alpha}(\omega)$, it can be shown with Eq. (48) that the population transfer rates in the opposite directions can be expressed as

$$K_{\beta\alpha} = \frac{2}{\hbar^{2}}\tilde{S}_{\beta\alpha}\left(\frac{E_{\beta} - E_{\alpha}}{\hbar}\right), \tag{49a}$$

$$K_{\alpha\beta} = \frac{2}{\hbar^2}\frac{\mathrm{Tr_b}[\exp\{-\beta(E_\alpha + \hat{V}_{\alpha\alpha})\}]}{\mathrm{Tr_b}[\exp\{-\beta(E_\beta + \hat{V}_{\beta\beta})\}]}\tilde{S}_{\beta\alpha}\left(\frac{E_\beta - E_\alpha}{\hbar}\right). \tag{49b}$$

Hence, the ratio between the two rate constants becomes

$$\frac{K_{\alpha\beta}}{K_{\beta\alpha}} = \frac{\mathrm{Tr_b}[\exp\{-\beta(E_\alpha + \hat{V}_{\alpha\alpha})\}]}{\mathrm{Tr_b}[\exp\{-\beta(E_\beta + \hat{V}_{\beta\beta})\}]}. \tag{50}$$

We then move on to the dissipation and apply a similar procedure to $\mathscr{S}^j_{\beta\alpha}(t')$ [Eq. (37)] to deduce

$$\mathscr{S}_{\beta\alpha}(t' - i\hbar\beta) = -\frac{\mathrm{Tr_b}[\exp(-\beta\hat{V}_{\beta\beta})]}{\mathrm{Tr_b}[\exp(-\beta\hat{V}_{\alpha\alpha})]}[\mathscr{S}_{\alpha\beta}(t')]^*, \tag{51}$$

which leads to

$$\frac{\mathscr{K}^j_{\alpha\beta}}{\mathscr{K}^j_{\beta\alpha}} = -\frac{\mathrm{Tr_b}[\exp\{-\beta(E_\alpha + \hat{V}_{\alpha\alpha})\}]}{\mathrm{Tr_b}[\exp\{-\beta(E_\beta + \hat{V}_{\beta\beta})\}]}. \tag{52}$$

Equation (46) is now instantly validated by combining Eqs. (50) and (52).

D. Application to linearly coupled harmonic oscillator bath

As a concrete example, we apply the framework developed in Secs. II A and II B to analyze the dissipation by a bath of quantum harmonic oscillators. In this case, the bath Hamiltonian takes the form

$$\hat{H}_\mathrm{B} = \sum_j \left(\frac{\hat{p}_j^2}{2} + \frac{\omega_j^2\hat{x}_j^2}{2}\right), \tag{53}$$

where $\hat{p}_j$ and $\hat{x}_j$ are the mass-weighted momentum and position operators for the jth bath mode, and ω_j is the characteristic frequency. We assume that the coupling between the subsystem and individual bath modes linearly depends on the positional coordinates, such that

$$\hat{H}_\mathrm{SB} = -\sum_A\sum_B\left(|A\rangle\langle B| \otimes \sum_j (\omega_j^2 d^j_{AB}\hat{x}_j + \gamma^j_{AB})\right), \tag{54}$$

where d^j_{AB} determines the strength of the subsystem–bath interaction and γ^j_{AB} accounts for the possible energy shift that arises from the freedom of setting the boundary between the subsystem and the bath [Eqs. (1) and (2)]. The profile of the subsystem–bath coupling in the frequency domain is contained in the spectral densities (SPDs),

$$J_{AB,CD}(\omega) = \sum_j \frac{\omega_j^3 d^j_{AB} d^j_{CD}}{2}\delta(\omega - \omega_j). \tag{55}$$

which can take into account both independent ($A = C$ and $B = D$) and correlated ($A \neq C$ or $B \neq D$) quantum fluctuations induced by the subsystem–bath interaction.

By converting Eqs. (53) and (54) to the exciton basis according to Eq. (6), we can specify the form of the bath-related operators in Eq. (8) as

$$\hat{v}^j_{\alpha\beta} = \left(\frac{\hat{p}_j^2}{2} + \frac{\omega_j^2\hat{x}_j^2}{2}\right)\delta_{\alpha\beta} - \omega_j^2 d^j_{\alpha\beta}\hat{x}_j + \gamma^j_{\alpha\beta}, \tag{56}$$

where $\delta_{\alpha\beta}$ is the Kronecker delta and

$$d^j_{\alpha\beta} = \sum_A\sum_B c^*_{\alpha A}c_{\beta B}d^j_{AB}, \tag{57a}$$

$$\gamma^j_{\alpha\beta} = \sum_A\sum_B c^*_{\alpha A}c_{\beta B}\gamma^j_{AB} \tag{57b}$$

are the coupling strengths and energy shifts in the exciton basis, respectively.

1. Population transfer

Based on Eq. (56), the rate constants for population transfer rate [Eq. (23)] and dissipation [Eq. (36)] can be computed by following the procedure illustrated in Secs. II A and II B, respectively.

To simplify the expressions that will appear in the derivations, we take an exciton state $|\alpha\rangle$ as a reference and redefine the positional coordinate according to $\hat{y}_j = \hat{x}_j - d^j_{\alpha\alpha}$ so that the origin $\hat{y}_j = 0$ coincides with the minimum of the PES $\hat{v}^j_{\alpha\alpha}$. In this new coordinate, Eq. (56) transforms into four different forms depending on which part of the subsystem the bath-related operators couple to

$$\hat{v}^j_{\alpha\alpha} = \frac{\hat{p}_j^2}{2} + \frac{\omega_j^2\hat{y}_j^2}{2} - \lambda^j_{\alpha\alpha,\alpha\alpha} + \gamma^j_{\alpha\alpha}, \tag{58a}$$

$$\hat{v}^j_{\beta\beta} = \frac{\hat{p}_j^2}{2} + \frac{\omega_j^2}{2}[\hat{y}_j - (d^j_{\beta\beta} - d^j_{\alpha\alpha})]^2 - \lambda^j_{\beta\beta,\beta\beta} + \gamma^j_{\beta\beta}, \tag{58b}$$

$$\hat{v}^j_{\alpha\beta} = -\omega_j^2 d^j_{\alpha\beta}\hat{y}_j - 2\lambda^j_{\alpha\beta,\alpha\alpha} + \gamma^j_{\alpha\beta}, \tag{58c}$$

$$\hat{v}^j_{\beta\alpha} = -\omega_j^2 d^j_{\beta\alpha}\hat{y}_j - 2\lambda^j_{\beta\alpha,\alpha\alpha} + \gamma^j_{\beta\alpha}, \tag{58d}$$

where $\alpha \neq \beta$ and $\lambda^j_{\mu\nu,\xi\chi} = \omega_j^2 d^j_{\mu\nu}d^j_{\xi\chi}/2$.

To obtain the rate constants for exciton population transfer [Eq. (16)], we need to compute $S_{\beta\alpha}(t')$ [Eq. (23)], which requires evaluating the traces in Eq. (22) using the bath-related operators defined in Eq. (58). To evaluate these traces, we begin with $\mathrm{Tr}0^j_{\beta\alpha}$ [Eq. (22a)], whose analytical expression,

$$\mathrm{Tr}0^j_{\beta\alpha} = \exp\left(-\frac{it'(\Delta^j_{\beta\alpha} + G^j_{\beta\alpha})}{\hbar} - \frac{G^j_{\beta\alpha}}{\hbar}f(\omega_j, t')\right), \tag{59}$$

was obtained using the generalized cumulant expansion technique[22,23] or the small polaron transformation.[24,25] Here, $G^j_{\beta\alpha}$, $\Delta^j_{\beta\alpha}$, and $f(\omega, t')$ are defined as

$$G^j_{\beta\alpha} = \lambda^j_{\alpha\alpha,\alpha\alpha} - 2\lambda^j_{\alpha\alpha,\beta\beta} + \lambda^j_{\beta\beta,\beta\beta}, \tag{60}$$

$$\Delta^j_{\beta\alpha} = \lambda^j_{\alpha\alpha,\alpha\alpha} - \lambda^j_{\beta\beta,\beta\beta} - \gamma^j_{\alpha\alpha} + \gamma^j_{\beta\beta}, \tag{61}$$

$$f(\omega,t') = \coth\left(\frac{\beta\hbar\omega}{2}\right)\frac{1-\cos(\omega t')}{\omega} + i\frac{\sin(\omega t') - \omega t'}{\omega}. \quad (62)$$

As shown in Appendix A, the analytical expression for the rest of the traces in Eq. (22) can be obtained as

$$\mathrm{Tr}1^j_{\beta\alpha} = -[i(\lambda^j_{\alpha\beta,\beta\beta} - \lambda^j_{\alpha\beta,\alpha\alpha})\dot{f}(\omega_j,t) + 2\lambda^j_{\alpha\beta,\alpha\alpha} - \gamma^j_{\alpha\beta}]\ \mathrm{Tr}0^j_{\beta\alpha}, \quad (63a)$$

$$\mathrm{Tr}2^j_{\beta\alpha} = -[i(\lambda^j_{\beta\alpha,\beta\beta} - \lambda^j_{\beta\alpha,\alpha\alpha})\dot{f}(\omega_j,t) + 2\lambda^j_{\beta\alpha,\alpha\alpha} - \gamma^j_{\beta\alpha}]\ \mathrm{Tr}0^j_{\beta\alpha}, \quad (63b)$$

$$\begin{aligned}\mathrm{Tr}3^j_{\beta\alpha} = \Big[&\{i(\lambda^j_{\alpha\beta,\beta\beta} - \lambda^j_{\alpha\beta,\alpha\alpha})\dot{f}(\omega_j,t) + 2\lambda^j_{\alpha\beta,\alpha\alpha} - \gamma^j_{\alpha\beta}\}\\ &\times\{i(\lambda^j_{\beta\alpha,\beta\beta} - \lambda^j_{\beta\alpha,\alpha\alpha})\dot{f}(\omega_j,t) + 2\lambda^j_{\beta\alpha,\alpha\alpha} - \gamma^j_{\beta\alpha}\}\\ &+ \hbar\lambda^j_{\alpha\beta,\beta\alpha}\ddot{f}(\omega_j,t')\Big]\ \mathrm{Tr}0^j_{\beta\alpha}. \end{aligned} \quad (63c)$$

Equations (59) and (63) allow us to construct the building blocks for $S_{\beta\alpha}(t')$ [Eq. (25)] as

$$W_{\beta\alpha}(t') = -i\hbar\{\dot{g}_{\alpha\beta,\beta\beta}(t') - \dot{g}_{\alpha\beta,\alpha\alpha}(t')\} - 2\Lambda_{\alpha\beta,\alpha\alpha} + \Gamma_{\alpha\beta}, \quad (64a)$$

$$X_{\beta\alpha}(t') = -i\hbar\{\dot{g}_{\beta\alpha,\beta\beta}(t') - \dot{g}_{\beta\alpha,\alpha\alpha}(t')\} - 2\Lambda_{\beta\alpha,\alpha\alpha} + \Gamma_{\beta\alpha}, \quad (64b)$$

$$Y_{\beta\alpha}(t') - Z_{\beta\alpha}(t') = \hbar^2\ddot{g}_{\alpha\beta,\beta\alpha}(t'), \quad (64c)$$

$$\begin{aligned}\Pi_{\beta\alpha}(t') = \exp\Big(&-\frac{it'}{\hbar}(2\Lambda_{\alpha\alpha,\alpha\alpha} - 2\Lambda_{\alpha\alpha,\beta\beta} - \Gamma_{\alpha\alpha} + \Gamma_{\beta\beta})\\ &- \dot{g}_{\alpha\alpha,\alpha\alpha}(t') + 2\dot{g}_{\alpha\alpha,\beta\beta}(t') - \dot{g}_{\beta\beta,\beta\beta}(t')\Big), \end{aligned} \quad (64d)$$

where we have defined the sum of $\lambda^j_{\mu\nu,\xi\chi}$ and $\gamma^j_{\mu\nu}$ over all bath components as

$$\Lambda_{\mu\nu,\xi\chi} = \sum_j \lambda^j_{\mu\nu,\xi\chi}, \quad \Gamma_{\mu\nu} = \sum_j \gamma^j_{\mu\nu}, \quad (65)$$

respectively, and the exciton line-broadening function,

$$g_{\mu\nu,\xi\chi}(t') = \frac{1}{\hbar}\sum_j\left[\lambda^j_{\mu\nu,\xi\chi}f(\omega_j,t')\right] = \frac{1}{\hbar}\int_{-\infty}^{\infty}\frac{J_{\mu\nu,\xi\chi}(\omega)}{\omega}f(\omega,t')\,d\omega, \quad (66)$$

where we have introduced the SPD in the exciton basis,

$$J_{\mu\nu,\xi\chi}(\omega) = \sum_j \frac{\omega_j^3 d^j_{\mu\nu}d^j_{\xi\chi}}{2}\delta(\omega-\omega_j). \quad (67)$$

The rate constants for population transfer can now be evaluated by plugging $S_{\beta\alpha}(t')$ [Eqs. (25) and (64)] in Eq. (15) and integrating numerically.

To further check the validity of the above expressions, we show that they correctly reproduce the already known results from modified Redfield theory[20,26] (MRT) when applied to a system of interacting chromophore molecules. For each chromophore, we only consider the ground and the first electronic excited states, whose energy difference ("site energy") undergoes fluctuations induced by interactions with the harmonic vibrational modes. We then take the diabatic state $|A\rangle$ to describe the situation in which only the chromophore A is electronically excited, while the rest remain in their ground state. The MRT assumes the Condon approximation,[27] which declares that the electronic couplings between the diabatic states are not affected by the vibrational degrees of freedom. This is equivalent to setting $d^j_{AB} = 0$ when $A \neq B$, with which Eq. (57) reduces to

$$d^j_{\alpha\beta} = \sum_A c^*_{\alpha A}c_{\beta A}d^j_{AA}. \quad (68)$$

The MRT also sets the diagonal elements of the subsystem Hamiltonian [Eq. (2)] as the vertical excitation energies at the minimum of the ground state PES, which makes $\gamma^j_{\mu\nu} = 0$ for all the bath modes and, subsequently, $\Gamma_{\mu\nu} = 0$ for all exciton state pairs μ and ν. Applying these conditions to $S_{\alpha\beta}(t')$ by using Eq. (64), the result is

$$S_{\beta\alpha}(t') = \mathscr{N}_{\beta\alpha}(t')\exp\left(-\frac{2it'}{\hbar}\Lambda_{\alpha\alpha,\alpha\alpha} - g_{\alpha\alpha,\alpha\alpha}(t') - g_{\beta\beta,\beta\beta}(t')\right), \quad (69)$$

where we have defined $\mathscr{N}_{\beta\alpha}(t')$ as

$$\begin{aligned}\mathscr{N}_{\beta\alpha}(t') = \exp\Big(&\frac{2it'}{\hbar}\Lambda_{\alpha\alpha,\beta\beta} + 2g_{\alpha\alpha,\beta\beta}(t')\Big)\\ &\times\big(-[\hbar\{\dot{g}_{\alpha\beta,\beta\beta}(t') - \dot{g}_{\alpha\beta,\alpha\alpha}(t')\} - 2i\Lambda_{\alpha\beta,\alpha\alpha}]\\ &\times[\hbar\{\dot{g}_{\beta\alpha,\beta\beta}(t') - \dot{g}_{\beta\alpha,\alpha\alpha}(t')\} - 2i\Lambda_{\beta\alpha,\alpha\alpha}]\\ &+\hbar^2\ddot{g}_{\alpha\beta,\beta\alpha}(t')\big). \end{aligned} \quad (70)$$

Inserting Eq. (69) into Eq. (16) gives

$$K_{\beta\alpha} = \frac{2}{\hbar^2}\ \mathrm{Re}\int_0^\infty \mathscr{F}^*_\alpha(t')\mathscr{N}_{\beta\alpha}(t')\mathscr{A}_\beta(t')\,dt', \quad (71)$$

where

$$\mathscr{F}_\alpha(t') = \exp\left[-\frac{it'(E_{\alpha 0} - \Lambda_{\alpha\alpha,\alpha\alpha})}{\hbar} - g^*_{\alpha\alpha,\alpha\alpha}(t')\right], \quad (72a)$$

$$\mathscr{A}_\beta(t') = \exp\left[-\frac{it'(E_{\beta 0} + \Lambda_{\beta\beta,\beta\beta})}{\hbar} - g_{\beta\beta,\beta\beta}(t')\right], \quad (72b)$$

$$\begin{aligned}\mathscr{N}_{\beta\alpha}(t') = \exp\Big(&\frac{2it'}{\hbar}\Lambda_{\alpha\alpha,\beta\beta} + 2g_{\alpha\alpha,\beta\beta}(t')\Big)\times\big(-\big[\hbar\big\{\dot{g}_{\alpha\beta,\beta\beta}(t')\\ &-\dot{g}_{\alpha\beta,\alpha\alpha}(t')\big\} - 2i\Lambda_{\alpha\beta,\alpha\alpha}\big]\times\big[\hbar\{\dot{g}_{\beta\alpha,\beta\beta}(t') - \dot{g}_{\beta\alpha,\alpha\alpha}(t')\}\\ &-2i\Lambda_{\beta\alpha,\alpha\alpha}\big] + \hbar^2\ddot{g}_{\alpha\beta,\beta\alpha}(t')\big), \end{aligned} \quad (72c)$$

which are in accord with the expressions for MRT reported in Ref. 20. Note that we have defined the zero-phonon exciton energies as

$$E_{\mu 0} = E_\mu - \Lambda_{\mu\mu,\mu\mu}. \quad (73)$$

2. Dissipation

Our next objective is to calculate the dissipation rate constants [Eq. (36)], for which the most crucial quantity is $\mathscr{D}^j_{\beta\alpha}(t')$ [Eq. (37)]. We first insert Eqs. (59) and (63) in Eq. (38) to derive concrete

expressions for the traces that are additionally required to calculate the dissipation,

$$\mathrm{Tr}4^{j}_{\beta\alpha} = [\Delta^{j}_{\beta\alpha} + G^{j}_{\beta\alpha} + iG^{j}_{\beta\alpha}\dot{f}(\omega_j, t')]\,\mathrm{Tr}0^{j}_{\beta\alpha}, \tag{74a}$$

$$\mathrm{Tr}5^{j}_{\beta\alpha} = [\Delta^{j}_{\beta\alpha} + G^{j}_{\beta\alpha} + iG^{j}_{\beta\alpha}\dot{f}(\omega_j, t')]\,\mathrm{Tr}1^{j}_{\beta\alpha} + \hbar(\lambda^{j}_{\alpha\beta,\beta\beta} - \lambda^{j}_{\alpha\beta,\alpha\alpha})\ddot{f}(\omega_j, t')\,\mathrm{Tr}0^{j}_{\beta\alpha}, \tag{74b}$$

$$\mathrm{Tr}6^{j}_{\beta\alpha} = [\Delta^{j}_{\beta\alpha} + G^{j}_{\beta\alpha} + iG^{j}_{\beta\alpha}\dot{f}(\omega_j, t')]\,\mathrm{Tr}2^{j}_{\beta\alpha} + \hbar(\lambda^{j}_{\beta\alpha,\beta\beta} - \lambda^{j}_{\beta\alpha,\alpha\alpha})\ddot{f}(\omega_j, t')\,\mathrm{Tr}0^{j}_{\beta\alpha}, \tag{74c}$$

$$\begin{aligned}\mathrm{Tr}7^{j}_{\beta\alpha} = {} & [\Delta^{j}_{\beta\alpha} + G^{j}_{\beta\alpha} + iG^{j}_{\beta\alpha}\dot{f}(\omega_j, t')]\,\mathrm{Tr}3^{j}_{\beta\alpha} \\ & + \hbar(\lambda^{j}_{\alpha\beta,\beta\beta} - \lambda^{j}_{\alpha\beta,\alpha\alpha})\ddot{f}(\omega_j, t')\,\mathrm{Tr}2^{j}_{\beta\alpha} \\ & + \hbar(\lambda^{j}_{\beta\alpha,\beta\beta} - \lambda^{j}_{\beta\alpha,\alpha\alpha})\ddot{f}(\omega_j, t')\,\mathrm{Tr}1^{j}_{\beta\alpha} \\ & + i\hbar^2\lambda_{\alpha\beta,\beta\alpha}f^{(3)}(\omega_j, t')\,\mathrm{Tr}0^{j}_{\beta\alpha},\end{aligned} \tag{74d}$$

where the traces in the right-hand sides of the equations are kept in their abbreviated form for compactness. If we substitute the traces in Eq. (39) with the corresponding expressions in Eq. (74), it can be noticed that some simplifications can be made by utilizing Eq. (26) and

$$(\mathrm{Tr}0^{j}_{\beta\alpha}X^{j-}_{\beta\alpha} + \mathrm{Tr}1^{j}_{\beta\alpha})\Pi^{j-}_{\beta\alpha} = X_{\beta\alpha}\Pi_{\beta\alpha}, \tag{75a}$$

$$(\mathrm{Tr}0^{j}_{\beta\alpha}W^{j-}_{\beta\alpha} + \mathrm{Tr}2^{j}_{\beta\alpha})\Pi^{j-}_{\beta\alpha} = W_{\beta\alpha}\Pi_{\beta\alpha}, \tag{75b}$$

which can be deduced from Eqs. (24) and (27). As a result, we get

$$\begin{aligned}\mathscr{S}^{j}_{\beta\alpha}(t') = {} & [\Delta^{j}_{\beta\alpha} + G^{j}_{\beta\alpha} - iG^{j}_{\beta\alpha}\dot{f}(\omega_j, t')]S_{\beta\alpha}(t') \\ & + \Big[\hbar(\lambda^{j}_{\beta\alpha,\beta\beta} - \lambda^{j}_{\beta\alpha,\alpha\alpha})\ddot{f}(\omega_j, t')W_{\beta\alpha}(t') \\ & + \hbar(\lambda^{j}_{\alpha\beta,\beta\beta} - \lambda^{j}_{\alpha\beta,\alpha\alpha})\ddot{f}(\omega_j, t')X_{\beta\alpha}(t') \\ & + i\hbar^2\lambda^{j}_{\alpha\beta,\beta\alpha}f^{(3)}(\omega_j, t')\Big]\Pi_{\beta\alpha}(t'),\end{aligned} \tag{76}$$

in which the concrete expressions for the time profiles on the right-hand side are given by Eqs. (24) and (64).

If all individual bath modes locally couple to a specific site, we can obtain a continuous expression for the rate of dissipation at each site within the frequency window $[\omega, \omega + d\omega]$ at a certain time. This is achieved by introducing the substitution,

$$\lambda^{j}_{\beta\alpha,\gamma\delta} \to \frac{J^{A}_{\beta\alpha,\gamma\delta}(\omega)}{\omega}d\omega, \tag{77}$$

for the bath modes associated with site A. After this procedure, the rate of dissipation at site A becomes

$$\mathscr{D}_A(\omega, t)\,d\omega = \sum_{\alpha}\sum_{\beta\neq\alpha}\mathscr{J}^{A}_{\beta\alpha}(\omega)P_\alpha(t)\,d\omega, \tag{78}$$

where $\mathscr{J}^{A}_{\beta\alpha}(\omega)$ is analogously defined as the expression in Eq. (36) but should be calculated by incorporating the aforementioned substitution [Eq. (77)].

This formalism shares a structural similarity with the previously developed QME-D method [see Eqs. (18) and (19) in Ref. 14], but also features some fundamental distinctions. In particular, the present formalism is developed in the exciton basis using the subsystem–bath coupling as the perturbation, while QME-D operates in the diabatic basis and treats the inter-site coupling within the subsystem as the perturbation. A further distinction lies in the complexity of the final dissipation rate expressions. The current approach, by construction, generates additional terms dependent on higher-order time derivatives of the bath response function [the final three terms in Eq. (76)]. These terms, which do not have a counterpart in QME-D, allow for a more detailed description of the dissipative dynamics at the cost of a more computationally demanding implementation.

The accumulated site dissipation at a given time, $\mathscr{E}_A(\omega, t)$, can then be obtained as

$$\mathscr{E}_A(\omega, t) = \int_0^t \mathscr{D}_A(\omega, t')dt'. \tag{79}$$

In turn, the total time-dependent dissipation can be obtained as

$$\mathscr{E}(\omega, t) = \sum_{A=1}^{N}\mathscr{E}_A(\omega, t), \tag{80}$$

where N is the number of sites.

III. RESULTS AND DISCUSSION

To evaluate the numerical accuracy of the proposed theoretical framework to capture dissipation, we will present results from a comprehensive set of simulations and compare them against benchmark data obtained using the HEOM,[28–30] specifically through the HEOM-D[31] approach that enables computing dissipation by individual components of the bath. We focus on dissipation dynamics within representative open quantum system models that feature harmonic bath modes, as detailed in Sec. II D. However, it is important to reiterate that the developed framework maintains its applicability to a broader range of environments, whether harmonic or anharmonic, provided they consist of independent bath degrees of freedom.

The subsystem–bath interactions in these simulations are primarily characterized by the widely used Drude–Lorentz (DL) and Brownian oscillator (BO) SPDs, defined in the diabatic basis. The DL SPD, which is often employed to describe the collective low-frequency motions of a solvent environment, is expressed as

$$J_{\mathrm{DL}}(\omega) = \frac{2\Lambda}{\pi}\frac{\omega_c\omega}{\omega^2 + \omega_c^2}, \tag{81}$$

where Λ is the total reorganization energy, which measures the overall strength of the subsystem–bath coupling, and ω_c is the cutoff frequency, which dictates the characteristic relaxation timescale of these bath modes. In turn, the BO SPD is typically used for modeling intramolecular vibrational modes of the molecule with a certain characteristic frequency. Its mathematical form is

$$J_{\mathrm{BO}}(\omega) = \frac{2\Lambda\gamma}{\pi}\frac{2\omega_0^2\omega}{(\omega^2 - \omega_0^2)^2 + 4\gamma^2\omega^2}, \tag{82}$$

where ω_0 is the frequency of the intramolecular vibration and γ is the damping strength.

The section is structured around four distinct sets of simulations, each designed to probe different aspects and parameter dependencies of the open quantum system dynamics. For the rest of this paper, all simulation parameters will be represented in Planck atomic units where $\hbar = k_B = 1$.

- **Simulation set A** focuses on a molecular dimer $(N = 2)$ where each site interacts with its own low-frequency bath components, as described by the DL SPD detailed above. In this case, the explicit expressions for the Hamiltonian components are

$$\hat{H}_S = \begin{pmatrix} \Delta E/2 & V \\ V & -\Delta E/2 \end{pmatrix}, \tag{83a}$$

$$\hat{H}_B = \sum_{A=1}^{N} \sum_j \left(\frac{\hat{P}_{Aj}^2}{2} + \frac{\omega_{Aj}^2 \hat{x}_{Aj}^2}{2} \right), \tag{83b}$$

$$\hat{H}_{SB} = -\sum_{A=1}^{N} \left(|A\rangle\langle A| \otimes \sum_j \omega_{Aj}^2 d_{Aj} \hat{x}_{Aj} \right). \tag{83c}$$

  Here, the extra index A of the bath-related quantities and operators reflects that each bath mode is exclusively coupled to a single subsystem state. Key parameters such as the inter-site coupling $(V = 0.25)$, temperature $(T = 1.0)$, and the DL cutoff frequency $(\omega_c = 0.5)$ are held constant. Meanwhile, we vary the reorganization energy Λ across values of $\{0.05, 0.2, 1.0, 2.0\}$ and the energy gap ΔE among $\{0.5, 1.0, 2.0\}$. For all 12 conditions within this set, the initial excitation is placed at the upper exciton state. Here, "upper exciton state" refers to the highest-energy eigenstate of Eq. (5), so that the initial exciton populations are $P_\alpha(0) = 0$ and $P_\beta(0) = 1$, given that $E_\alpha < E_\beta$.
- **Simulation set B** utilizes the same molecular dimer model as simulation set A [Eq. (83)], but investigates the effects of varying temperature instead. Key parameters such as the inter-site coupling $(V = 0.25)$, reorganization energy $(\Lambda = 0.2)$, and the DL cutoff frequency $(\omega_c = 0.5)$ are held constant, while we vary the temperature T across values of $\{0.25, 0.5, 1.0\}$ and the energy gap ΔE among $\{0.5, 1.0, 2.0\}$. For all nine conditions within this set, the initial excitation is placed at the upper exciton state.
- **Simulation set C** examines a spin-boson model that represents a two-level subsystem $(N = 2)$ coupled to a single bath. In this case, the Hamiltonian components $\hat{H}_S$ and $\hat{H}_B$ are given by Eqs. (83a) and (53), respectively, while $\hat{H}_{SB}$ takes the form of

$$\hat{H}_{SB} = \begin{pmatrix} 1 & 0 \\ 0 & -1 \end{pmatrix} \otimes \left(\sum_j \omega_j^2 d_j \hat{x}_j \right). \tag{84}$$

  The subsystem–bath interaction is characterized by the BO SPD detailed above. Key parameters such as the inter-site coupling $(V = 0.25)$, temperature $(T = 1.0)$, energy gap $(\Delta E = 2.0)$, and the BO characteristic frequency $(\omega_0 = 2.062)$ are held constant. In contrast, we vary the reorganization energy Λ across values of $\{0.05, 0.25, 1.0\}$ and the BO damping strength γ among $\{0.05, 0.25, 1.0\}$. For all nine conditions within this set, the initial excitation is placed at the upper exciton state.
- **Simulation set D** extends the analysis to a molecular trimer $(N = 3)$ where each site interacts with low-frequency components of the bath, described by the model Hamiltonian of Eq. (83) with the DL SPD detailed above. The matrix representation of the subsystem Hamiltonian $\hat{H}_S$ is

$$\hat{H}_S = \begin{pmatrix} 2.0 & V_{12} & 0.25 \\ V_{12} & 1.0 & 0.0 \\ 0.25 & 0.0 & 0.0 \end{pmatrix}, \tag{85}$$

  where the inter-site coupling V_{12} is varied among $\{0.25, 0.5, 1.0\}$, and the reorganization energy Λ among $\{0.1, 0.5\}$. The temperature T is maintained at 1.0, and the DL cutoff frequency ω_c is 0.5. The reorganization energy Λ is also varied across $\{0.1, 0.5\}$. Furthermore, three distinct initial excitation schemes are employed. The first scheme involves placing the initial excitation at site 2. This setup compares QME-D[14,19] results against HEOM benchmarks to demonstrate the regime of applicability of QME-D. The second scheme utilizes an incoherent mixture of exciton states corresponding to the initial excitation localized at site 2, which is chosen to show how our framework can overcome certain limitations inherent in QME-D. The third scheme places the initial excitation directly into the middle exciton state. This corresponds to $P_{\alpha=2}(0) = 1$ and $P_{\alpha=1}(0) = P_{\alpha=3}(0) = 0$ given that the exciton energies satisfy $E_{\alpha=1} < E_{\alpha=2} < E_{\alpha=3}$. There are a total of 18 distinct simulation conditions for this set.

A schematic of the model systems and SPDs used in this section is presented in Fig. 1.

To incorporate non-Markovian effects, we implemented the time scale separation (TSS) method.[32,33] This method separates the SPD into slow and fast components and only lets the fast component directly influence the subsystem dynamics, while the slow component is treated as a source of static disorder. The separation is formally achieved by defining

$$\begin{aligned} J_{\text{slow}}(\omega) &= S(\omega, \omega^*) J(\omega), \\ J_{\text{fast}}(\omega) &= [1 - S(\omega, \omega^*)] J(\omega), \end{aligned} \tag{86}$$

where $S(\omega, \omega^*)$ is the splitting function given by

$$S(\omega, \omega^*) = \begin{cases} \eta[1 - (\omega/\omega^*)^2]^2, & \omega < \omega^*, \\ 0, & \omega \geq \omega^*, \end{cases} \tag{87}$$

and ω^* is the cutoff frequency.

As the simulation sets described here are consistent with the modified Redfield theory, we will now refer to our method for computing dissipation as MRT-D. In Secs. III A–III C, the dissipation calculated by QME-D, MRT-D, and HEOM-D will be compared to investigate their regime of validity and limitations. In particular, for simulation set D, the direct contrast between QME-D and MRT-D

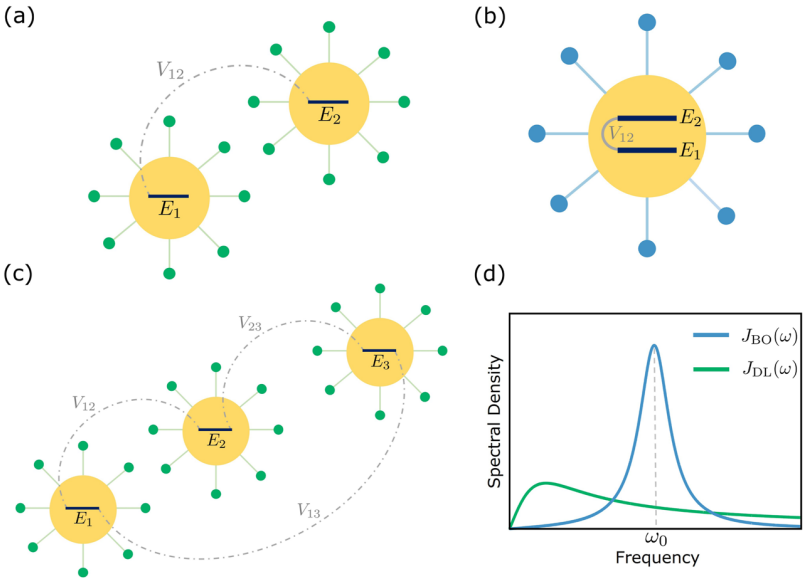

FIG. 1. Schematic representation of the model systems. (a) Molecular dimer model where each subsystem state (whose energies are labeled by E_1 and E_2) is connected to its own set of harmonic oscillator baths (represented by green circles). V_{12} is the inter-state coupling between the two subsystem states. (b) Spin-boson model where both subsystem states are simultaneously connected to a single set of harmonic oscillator baths (represented by blue circles). (c) Same as in (a) but for a molecular trimer model. (d) Plots of the Drude–Lorentz SPD [Eq. (81), green line] used for simulations of the molecular dimer/trimer and the Brownian oscillator SPD [Eq. (82), blue line] used for simulations of the spin-boson model.

will highlight the ability of MRT-D to handle delocalized exciton states that is absent in QME-D. In every set of simulations, for fair comparison, the initial conditions for the simulation methods are chosen as close as possible. However, it should be noted that the deviations between the bath densities cannot be eliminated due to the different projection operators used in QME-D and MRT-D, as well as the factorized initial condition assumed in HEOM-D.

A. Molecular dimer

1. Simulation details

For the MRT-D calculations involving simulation sets A and B, each DL SPD associated with the dimer sites was discretized into 2000 harmonic oscillator modes by following the scheme detailed in Appendix B. The upper limit of the frequency was set to be $\omega_{max} = 15$, which recovered 97.9% of the analytical reorganization energy of the SPD. Time integrals for determining the rate constants for the population transfer [Eq. (71)] and dissipation [Eq. (36)] were evaluated using the trapezoidal method with an integration grid size of 0.02 and an upper integration limit of 5×10^3. The coupled rate equations for exciton populations [Eq. (15)] were then propagated using a fourth-order Runge–Kutta algorithm with a time step of 0.02.

As noted previously, TSS was incorporated into MRT-D calculations to explore the influence of non-Markovian memory effects on the dynamics. For simulation sets A and B, the splitting function [Eq. (87)] was defined by setting $\eta = 0.99$ and $\omega^* = 0.05$. The final results were obtained by averaging over a number of trajectories that are enough to achieve numerical convergence. In particular, 10^4 trajectories were used for the conditions involving a reorganization energy $\Lambda = 0.05$ (part of simulation set A), while 10^3 trajectories were used for all other conditions within simulation sets A and B.

For comparison, numerically exact benchmarks for the dissipation dynamics were established using the HEOM. This was implemented using the HEOM-D strategy for monitoring bath components developed by Kim,[31] along with an efficient low-temperature correction scheme recently reported.[34] Key HEOM parameters for each simulation condition, including the hierarchy depth N_{hier}, the number of Matsubara terms N_{Matsu}, and the Huang–Rhys (H–R) factor for the probe mode s_{pb}, are detailed in Table I.

TABLE I. Parameters for simulation sets A and B (molecular dimer). The reorganization energy Λ and temperature T define the subsystem–bath interaction, while the remaining entries specify the HEOM procedure. Each of the six conditions listed was combined with three different values of energy gap $\Delta E = \{0.5, 1.0, 2.0\}$, resulting in 18 distinct sets of simulation parameters.

Simulation condition	(i)	(ii)	(iii)	(iv)	(v)	(vi)
Reorganization energy (Λ)	0.05	0.2	1.0	2.0	0.2	0.2
Temperature (T)	1.0	1.0	1.0	1.0	0.5	0.25
Maximum time step (Δt_{max})	0.02	0.1	0.05	0.05	0.1	0.1
Number of hierarchy tiers (N_{hier})	4	7	10	13	7	7
Number of Matsubara terms (N_{Matsu})	30	30	30	30	100	100
H–R factor of the probe mode (s_{pb})	2×10^{-6}	1×10^{-5}	1×10^{-5}	1×10^{-5}	1×10^{-5}	1×10^{-5}

The frequency of the HEOM-D probe mode was scanned from 0.2 to 3.0 in steps of 0.05. For probe frequencies $\omega \geq 0.3$, the number of vibrational quantum states describing the probe was chosen to ensure the initial bath density to represent 99.9% of the total Boltzmann population. This threshold was relaxed to 99.0% for $\omega < 0.3$ to mitigate the rapidly increasing computational burden at lower frequencies. The approach to steady-state ($t \to \infty$) was practically handled by defining a finite simulation time t_{sim} for each condition. This time was determined by visually inspecting the convergence of exciton population dynamics. The subsystem reduced density matrix (RDM) and the associated auxiliary density matrices (ADMs) were propagated using an adaptive RKF45 integrator.[35] The time step was dynamically adjusted based on the deviation of the trace of the RDM from unity. To further ensure numerical stability, especially near the steady state, the integration time step was not permitted to exceed a predefined maximum Δt_{max}.

2. Electronic dynamics

Accurate exciton populations are a fundamental prerequisite to reliably capturing energy dissipation dynamics. For this reason, we first examine the fidelity of the population dynamics predicted by MRT. We evaluate this accuracy by describing the time evolution of exciton populations within the molecular dimer and benchmarking the predictions of MRT against numerically exact HEOM results. This comparison is illustrated in Figs. 2 and 3 for simulation sets A and B, respectively, by displaying the time-dependent population inversion $\langle \hat{\sigma}_z(t) \rangle = P_\beta(t) - P_\alpha(t)$. Here, P_α and P_β are the populations for the lower and higher exciton states, respectively. Both figures compare MRT (cyan line) with HEOM (pink dashed line).

Figure 2 shows that MRT performs well across a wide range of conditions covered by simulation set A, yielding good agreement with HEOM. While MRT provides good predictions in general, some deviations from HEOM benchmarks emerge under specific conditions, notably highlighted in panels Figs. 2(b)–2(d) and 2(h). These cases exemplify situations with the reorganization energy $\Lambda \geq 0.2$ and the energy gap $\Delta E \leq 1.0$, under which MRT overestimates the rate of population transfer. The challenge for MRT is most apparent when strong subsystem–bath coupling ($\Lambda = 1.0$) combines with a small energy gap of $\Delta E = 0.5$ [Fig. 2(d)], where the accuracy falls short in precisely capturing the steady state and transfer rate. This behavior is attributed to the assumption underlying MRT that the subsystem–bath coupling strength is relatively small compared to ΔE.

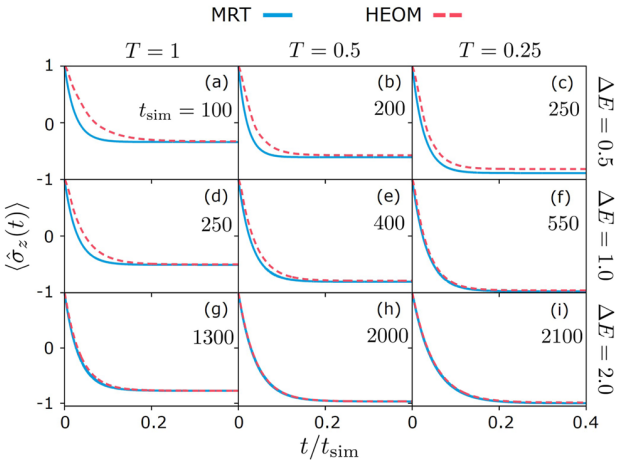

FIG. 3. Time-dependent population inversion for simulation set B (molecular dimer), with details specified in Sec. III A 1.

Conversely, the accuracy of MRT significantly improves as ΔE increases. This enhanced performance arises because a larger energy gap promotes more localized exciton states. Consequently, the dynamics becomes predominantly diffusive and is more adequately described by an incoherent exponential decay. This characteristic behavior becomes clearer by solving the coupled differential equations for state populations, Eq. (14), which leads to an analytical expression for the population inversion given by

$$\langle \hat{\sigma}_z(t) \rangle = \langle \hat{\sigma}_z(\infty) \rangle + [\langle \hat{\sigma}_z(0) \rangle - \langle \hat{\sigma}_z(\infty) \rangle] \exp(K_{\beta\alpha} - K_{\alpha\beta})t. \quad (88)$$

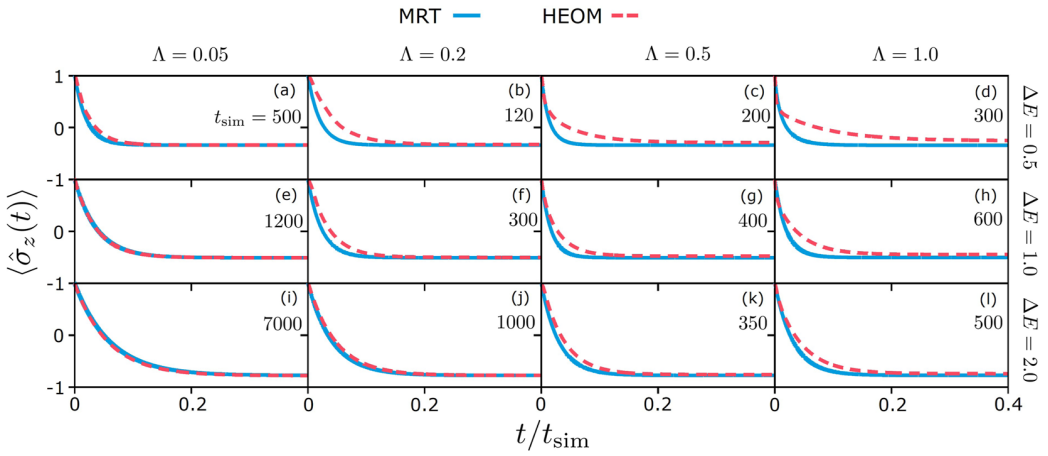

FIG. 2. Time-dependent population inversion for simulation set A (molecular dimer), with details specified in Sec. III A 1.

Figure 3 presents the results for simulation set B, whose trends are similar to those in Fig. 2. That is, the accuracy of MRT improves with increasing ΔE, while the population transfer rates are slightly overestimated as the energy gap is reduced and the temperature is increased. Such deviations are attributed to greater thermal fluctuations induced by the subsystem–bath interaction.

3. Dissipation dynamics

Having addressed the performance of MRT for population dynamics in Sec. III A 2, we now consider evaluating the dissipation predicted by MRT-D. We will compare these predictions against HEOM-D benchmarks for simulation sets A and B. We will focus on total dissipation to maintain visual clarity in the analysis. A more detailed examination of site-specific dissipation contributions will be explored in the subsequent discussion of the molecular trimer system (Sec. III C).

The frequency-resolved dissipation can be accessed through the accumulated dissipation density, $\mathscr{E}(\omega, t)$, as defined in Eq. (80). Figure 4 illustrates the steady-state cumulative dissipation, $\mathscr{E}(\omega, \infty)$, for simulation set A, comparing the results obtained from MRT-D (cyan line) and HEOM-D (pink dashed line). The accuracy of MRT-D in predicting dissipation improves with decreasing reorganization energy Λ and increasing energy gap ΔE, which is consistent with the trends observed for population dynamics presented in Fig. 2. It is particularly noteworthy that even for the challenging condition of $\Lambda = 1.0$ and $\Delta E = 0.5$ [Fig. 4(d)], where MRT showed quantitative deviations in population dynamics, MRT-D still yields a qualitatively good description of the dissipation spectrum.

By examining the dissipation mechanisms revealed in Fig. 4, we observe distinct behaviors dependent on the subsystem–bath coupling strength. When the reorganization energy takes a relatively small value of $\Lambda = 0.05$, a substantial portion of the energy dissipation occurs through a channel centered around $\hbar\omega = \Delta E$. This feature can be attributed to vibronic resonance, where energy is efficiently transferred to quasi-resonant bath modes with the exciton energy difference. As the reorganization energy Λ is increased, the contribution of this vibronic resonance channel gradually diminishes, and the dissipation becomes increasingly concentrated at lower frequencies close to $\omega = 0$. This shift indicates that stronger coupling promotes dissipation into slower, collective bath motions.

In turn, Fig. 5 shows the influence of temperature on the total accumulated dissipation at the steady-state, $\mathscr{E}(\omega, \infty)$, for simulation set B, comparing MRT-D and HEOM-D calculations. The accuracy of MRT-D generally increases with a larger energy gap ΔE, and it successfully captures the correct qualitative trends across the temperature series. Notably, lowering the temperature from $T = 1.0$ to $T = 0.25$ enhances the prominence of the vibronic resonance channel in the dissipation spectrum. This enhancement results from the reduction in thermal fluctuations induced by the subsystem–bath interaction at lower temperatures, which allows the resonant energy transfer processes to become more dominant.

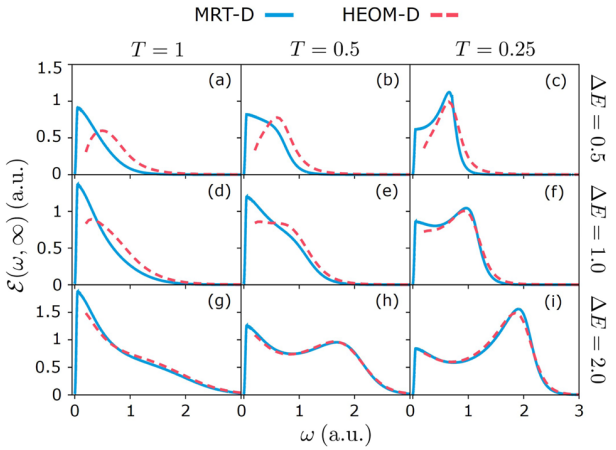

FIG. 5. Total steady-state dissipation density for simulation set B (molecular dimer), with details specified in Sec. III A 1.

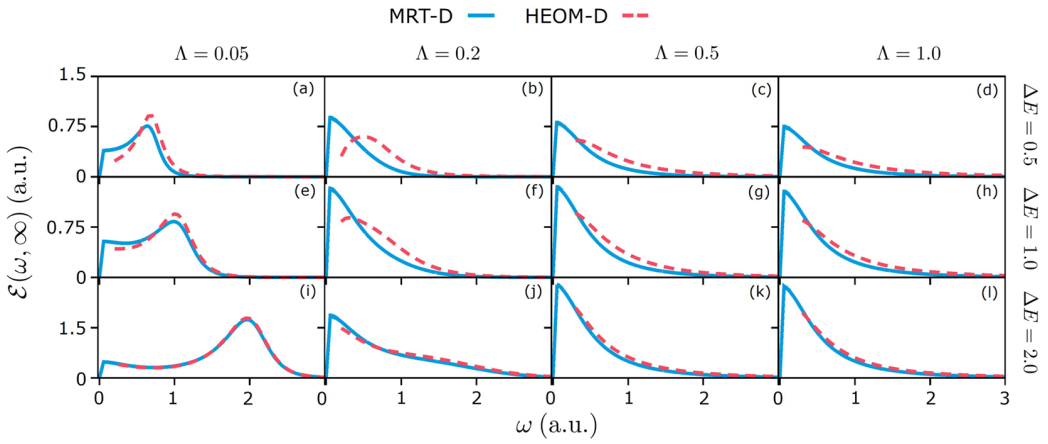

FIG. 4. Total steady-state dissipation density for simulation set A (molecular dimer), with details specified in Sec. III A 1.

B. Spin-boson model with Brownian oscillator bath

1. Simulation details

The spin-boson model (simulation set C) features a two-level subsystem coupled to a single bath, which is characterized by a BO SPD [Eq. (82)]. Key parameters such as the inter-site coupling ($V = 0.25$), temperature ($T = 1.0$), energy gap ($\Delta E = 2.0$), and the BO characteristic frequency ($\omega_0 = 2.062$) were held constant. We varied the reorganization energy Λ across values of $\{0.05, 0.25, 1.0\}$ and the BO damping strength γ among $\{0.05, 0.25, 1.0\}$. For all nine conditions within this set, the initial excitation was placed at the upper exciton state.

The BO SPD was discretized into 10 000 harmonic oscillator modes for the MRT-D computations. The discretization scheme follows the procedure described in Appendix B. In turn, we set $\omega_0 = 2.062$ as the center of the BO SPD. Time integrals for determining the rate constants for population transfer [Eq. (71)] and dissipation [Eq. (36)] were evaluated using the trapezoidal method with an integration grid size of 0.02 and an upper integration limit of 5×10^3. The coupled rate equations for exciton populations [Eq. (15)] were propagated using a fourth-order Runge–Kutta algorithm with a time step of 0.02.

For TSS, the splitting function [Eq. (87)] was defined by setting the cutoff frequency $\omega^* = 0.05$, and the parameter η was reduced from 0.99 (as used for simulation sets A and B) to 0.6. This reduction was necessary due to the increased difficulty of achieving detailed balance conditions with the BO SPD. To ensure numerical convergence, the number of individual trajectories averaged to obtain final results was kept at 10^4.

For the HEOM and HEOM-D simulations, we implemented the BO SPD based on Ref. 36 and applied the strategy for monitoring bath components developed by Kim,[31] along with an efficient low-temperature correction scheme recently reported.[34] The HEOM-D parameters used for each simulation condition can be found in Table I.

2. Electronic and dissipation dynamics

Figure 6 presents the time evolution of the population inversion $\langle \hat{\sigma}_z(t) \rangle$ for nine different simulation conditions in Table II, revealing the accuracy of MRT when benchmarked against HEOM results. For a small damping strength such as $\gamma = 0.05$, Figs. 6(a)–6(c) show that MRT faces challenges in describing the highly non-Markovian character of the bath dynamics. This difficulty arises from the underdamped nature of the bath, which leads to persistent memory effects. However, as the damping strength γ increases, the agreement between MRT and HEOM benchmarks improves significantly. MRT provides a nearly quantitative match to the benchmark electronic dynamics for larger values of γ (e.g., 0.25 and 1.0), showing its utility when the bath becomes more dissipative and its memory effects are shortened.

In Fig. 7, we present the steady-state accumulated dissipation density $\mathscr{E}(\omega, \infty)$ in MRT-D and HEOM-D. The results in Fig. 7 show that for small ($\gamma = 0.05$) and intermediate ($\gamma = 0.25$) damping strengths, most of the energy dissipation occurs through a resonant channel around $\omega \approx 2.0$. This frequency corresponds closely to both the subsystem energy gap ($\Delta E = 2.0$) and the characteristic frequency of the Brownian oscillator ($\omega_0 = 2.062$). An interesting

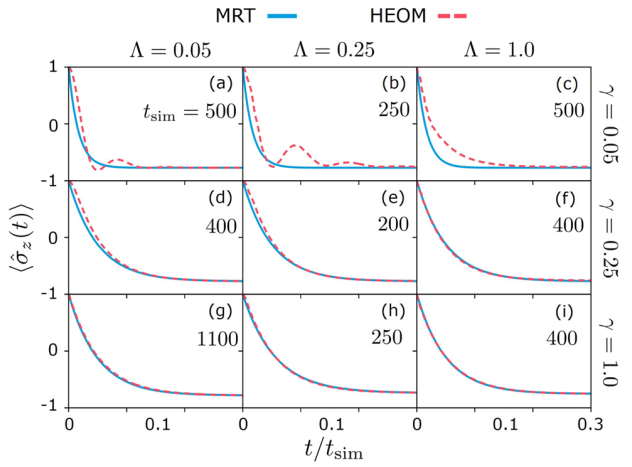

FIG. 6. Time-dependent population inversion for simulation set C (spin-boson model), with details specified in Sec. III B 1.

TABLE II. Parameters for simulation set C (spin-boson model). The reorganization energy Λ defines the subsystem–bath interaction, and the remaining entries specify the HEOM procedure. Each of the three conditions listed was combined with three different damping strengths, $\gamma = \{0.5, 1.0, 2.0\}$, resulting in nine distinct sets of simulation parameters.

Simulation condition	(i)	(ii)	(iii)
Reorganization energy (Λ)	0.05	0.25	1.0
Maximum time step ($\Delta t_{\max}$)	0.01	0.05	0.05
Number of hierarchy tiers (N_{hier})	5	7	12
Number of Matsubara terms (N_{Matsu})	10	15	25
H–R factor of the probe mode (s_{pb})	2×10^{-6}	1×10^{-5}	1×10^{-5}

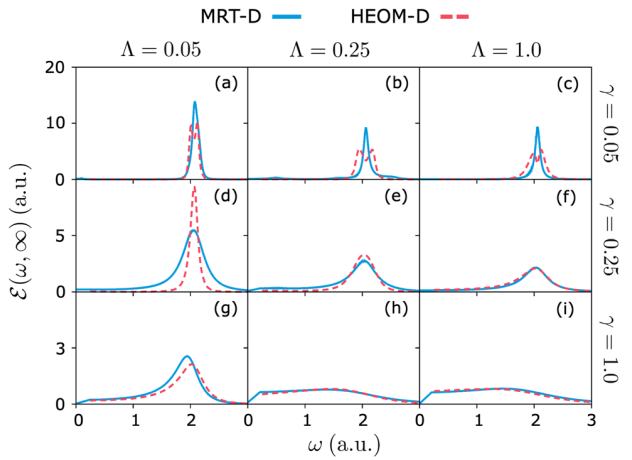

FIG. 7. Total steady-state dissipation density for simulation set C (spin-boson model), with details specified in Sec. III B 1.

feature observed with a very small damping strength of $\gamma = 0.05$ [Figs. 7(a)–7(c)] is that the dissipation spectrum in HEOM-D does not form a single peak, in contrast to the shape of the BO SPD itself. Instead, the dissipation spectra exhibit a pair of closely lying peaks. Such a structure arises from the strong coherent interaction between the upper subsystem state and the first excited state of the underdamped bath mode, a phenomenon analogous to the formation of polaritonic states. However, this distinct peak-splitting behavior diminishes and eventually disappears as the resonance effect is diluted due to increased damping strength.

For all conditions displayed in Fig. 7, MRT-D qualitatively reproduces the general features of the dissipation spectra obtained from HEOM-D calculations. The predictive capability of MRT-D improves with increasing damping strength, which enhances the accuracy of the Markov approximation. Interestingly, when the reorganization energy is small ($\Lambda = 0.05$), MRT-D deviates from the HEOM-D calculations. We attribute this behavior to the absence of low-frequency components in the bath, which leads to a long memory of the bath and consequently degrades the validity of the Markov approximation.

C. Molecular trimer

1. Simulation details

The simulations for the molecular trimer model (simulation set D) were performed using Planck atomic units ($\hbar = k_B = 1$). In this model, each site of the trimer interacts with its own low-frequency bath components, characterized by a DL SPD. Key fixed parameters for these simulations include a temperature ($T = 1.0$) and a DL cutoff frequency ($\omega_c = 0.5$). The inter-site energy gaps were set to $\Delta E_{12} = 1.0$, $\Delta E_{13} = 2.0$, and $\Delta E_{23} = 1.0$. Specific inter-site couplings are also set at $V_{13} = 0.25$ and $V_{23} = 0.0$. The simulations explored variations in the reorganization energy $\Lambda = \{0.1, 0.5\}$ and the inter-site coupling $V_{12} = \{0.25, 0.5, 1.0\}$. A total of 18 distinct simulation conditions were examined, encompassing three different initial excitation schemes. The first scheme involved placing the initial excitation at site 2 to compare QME-D results against HEOM-D benchmarks. This corresponds to the initial condition $P_{A=2}(0) = 1$. The second scheme utilized an incoherent mixture of exciton states, constructed by converting the initial excitation localized at site 2 to the exciton basis and only extracting the populations. This aims to show how MRT-D can overcome certain limitations inherent in QME-D. The third scheme placed the initial excitation directly at the middle exciton state, such that $P_{\alpha=2}(0) = 1$. The remaining computational details for QME(-D), MRT(-D), and HEOM(-D) were identical to those described in Sec. III A 1 and Table I.

2. Electronic dynamics

In this section, we investigate the electronic population dynamics of simulation set D. The primary goal is to demonstrate that MRT can accurately capture dynamics under conditions where QME becomes unreliable. As QME and MRT are formulated in different bases—the site and exciton bases, respectively—the HEOM benchmark results are presented in the appropriate basis for each comparison.

First, to illustrate the limitations of QME, we initialized the simulation with the excitation localized at site 2. The population dynamics are presented in Fig. 8, where solid lines represent the QME calculations and dashed lines depict the HEOM benchmarks (site 1: blue, site 2: green, and site 3: orange). As is evident from Fig. 8, QME accurately captures the population dynamics only under particular conditions of small electronic coupling ($V_{12} = 0.25$) and large reorganization energy ($\Lambda = 0.5$), as shown in Fig. 8(d). For the majority of other conditions tested [Figs. 8(a)–8(c) and 8(f)], QME fails to reproduce the correct dynamical behavior. Even in cases such as Fig. 8(e), where QME might eventually reach the correct steady-state populations, it fails to describe the short-time dynamics accurately.

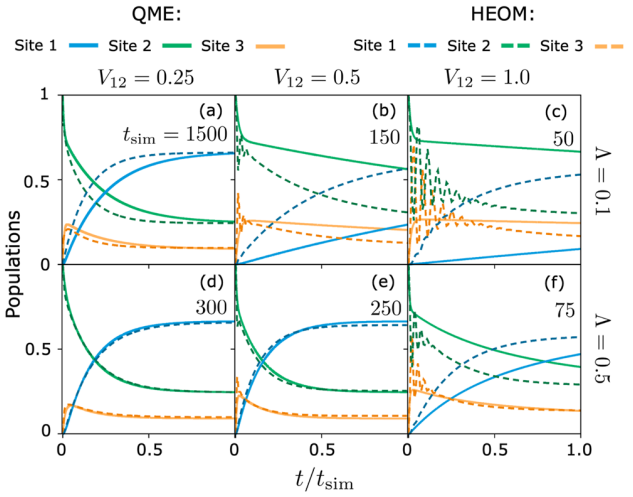

FIG. 8. Population dynamics for simulation set D (molecular trimer) with initial excitation localized at site 2. Details of the simulation are presented in Sec. III C 1.

To address these limitations, we examine the performance of MRT against HEOM. For this, we use an incoherent exciton initial condition that corresponds to an initial excitation localized at site 2. In Fig. 9, we show that the population dynamics predicted by MRT show a markedly improved agreement with HEOM across the simulation set. While some deviations emerge at strong electronic couplings, MRT consistently yields more accurate steady-state populations compared to QME.

Finally, motivated by the observation that MRT can effectively handle conditions challenging for QME, we tested an initial condition where the excitation is localized in the middle exciton energy state. The population dynamics for this scenario are shown in Fig. 10. The results again indicate good agreement between MRT and HEOM. This agreement persists until the electronic coupling becomes strong (e.g., $V_{12} = 1.0$); however, even under such strong coupling, the steady-state populations are still accurately predicted by MRT.

3. Dissipation dynamics

For dissipation, we first apply QME-D to the excitation initially localized at site 2. The resulting steady-state dissipation densities $\mathscr{E}(\omega, \infty)$ are presented in Fig. 11 for individual sites, comparing QME-D (solid lines) with HEOM-D (dashed lines). The QME-D results align with the HEOM-D benchmarks only under specific

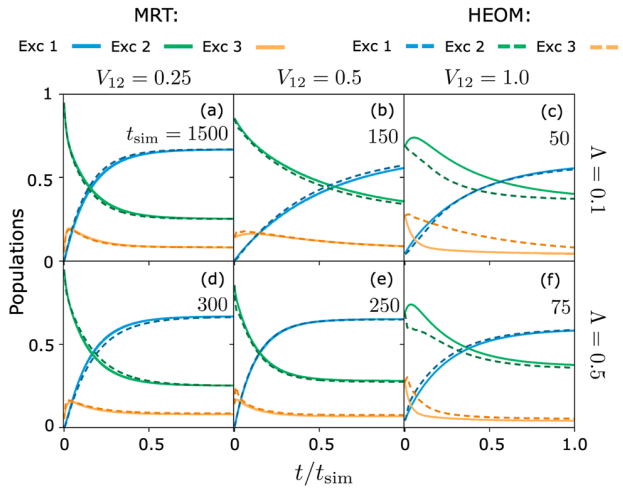

FIG. 9. Population dynamics for simulation set D (molecular trimer) starting from an incoherent exciton mixture corresponding to site 2. Details of the simulation are presented in Sec. III C 1.

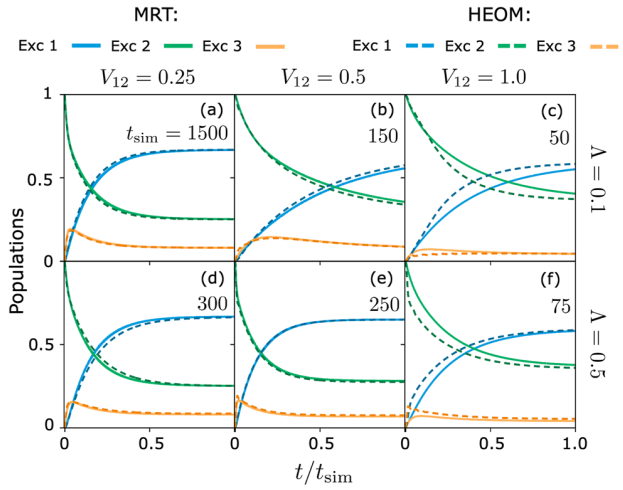

FIG. 10. Population dynamics for simulation set D (molecular trimer) with the initial excitation localized at the middle exciton state. Details of the simulation are presented in Sec. III C 1.

conditions, notably at $V_{12} = 0.25$ and $\Lambda = 0.5$ [Fig. 11(d)]. According to Sec. II, this agreement is expected, as these parameters favor the perturbative treatment with respect to the electronic coupling V, increasing the accuracy of QME-D. The electronic coupling V_{12} primarily scales the rate constants by V_{12}^2,[14] which uniformly affects the entire frequency range of the dissipation spectrum. Consequently, while increasing V_{12} speeds up the overall dissipation process, it does not significantly alter the qualitative features of the steady-state dissipation profiles within QME-D. However, for most other conditions, QME-D fails to accurately reproduce both the strength and shape of the site dissipation densities compared to the HEOM-D benchmarks. Furthermore, when $V_{12} = 1.0$, HEOM-D reveals a

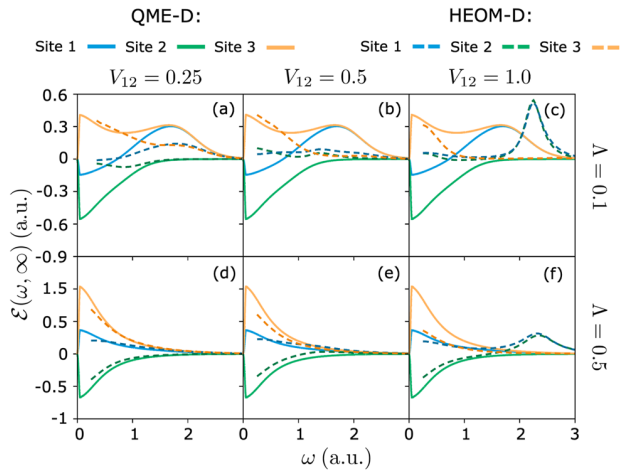

FIG. 11. Site-specific steady-state dissipation density for simulation set D (molecular trimer) with initial excitation localized at site 2. Details of the simulation are presented in Sec. III C 1.

structured peak at a higher frequency [Figs. 11(c) and 11(f)], which is close to the energy difference between the highest and lowest exciton states ($\omega \approx 2.7$). In contrast, QME-D does not capture this feature.

To address the limitations of QME-D, we now examine the results obtained with MRT-D. In Fig. 12, we show the steady-state dissipation densities when the initial condition is an incoherent mixture of excitons corresponding to site 2. The HEOM-D results in Fig. 12 are very similar to those in Fig. 11. For a broad range of parameters, each site dissipation density predicted by MRT-D closely follows the trends observed in the HEOM-D, including the resonant structure of the peaks previously missed by QME-D for $V_{12} = 1.0$. For $\Lambda = 0.1$, MRT-D provides quantitatively accurate

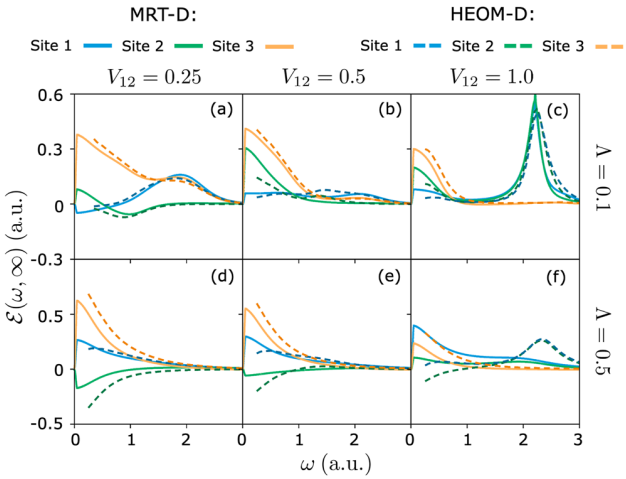

FIG. 12. Site-specific steady-state dissipation density for simulation set D (molecular trimer) using an incoherent exciton mixture corresponding to site 2. Details of the simulation are presented in Sec. III C 1.

results [Figs. 12(a)–12(c)], although some discrepancies emerge as the reorganization energy increases to $\Lambda = 0.5$ [Figs. 12(d)–12(f)]. Nevertheless, MRT-D still captures the correct qualitative trends for $V_{12} = 0.25$ [Fig. 12(d)] and $V_{12} = 0.5$ [Fig. 12(e)]. At strong inter-site coupling and high reorganization energy with $V_{12} = 1$ and $\Lambda = 0.5$ [Fig. 12(f)], MRT-D struggles to reproduce HEOM-D results.

Finally, we investigated the dissipation dynamics when the initial excitation is localized in the middle exciton state, with results shown in Fig. 13. While the specific dissipation profiles differ from those in Fig. 12 due to the different initial conditions, MRT-D continues to effectively retrieve the correct trends and structural features of the dissipation dynamics across most of the simulation conditions. The only exception is the challenging regime of strong electronic coupling $(V_{12} = 1)$ and large reorganization energy $(\Lambda = 0.5)$ [Fig. 13(f)], where deviations from HEOM-D are noticeable.

In summary, the MRT-D framework can reliably treat situations where QME-D is not suitable and enables the study of dissipation pathways across a broader range of simulation conditions. Importantly, while HEOM-D provides numerically exact results, its computational cost often limits its applicability to relatively small systems and baths with simple SPDs. By contrast, approximate methods such as QME-D and MRT-D offer a more scalable route to investigating dissipation in more complex molecular systems with highly structured environments.

D. Possible extensions to coherent dynamics

The theories of dissipation developed in the current work and our previous papers, I and II,[14,19] only follow the state populations, as in the QMEs from which they were derived.[20,26] However, as shown in Figs. 8(c) and 8(f), the off-diagonal elements of the density matrix (coherence) may significantly affect the dynamics when the inter-site couplings become large. Therefore, it will be meaningful if our theoretical framework could be further extended toward retaining the coherence during propagation.

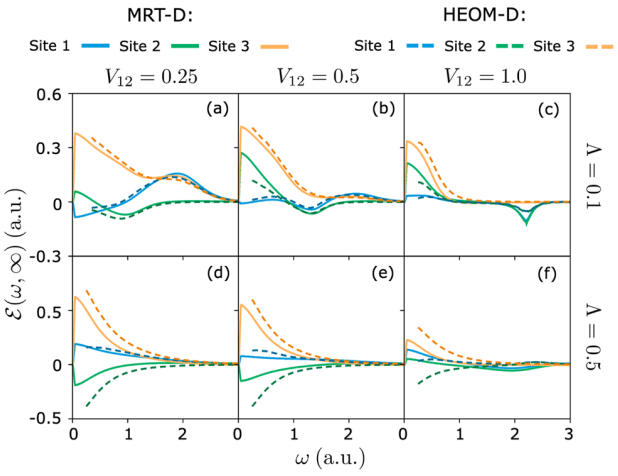

FIG. 13. Site-specific steady-state dissipation density for simulation set D (molecular trimer) with the initial excitation localized at the middle exciton state. Details of the simulation are presented in Sec. III C 1.

Recently, there have been studies that successfully incorporated coherences in QMEs under the Nakajima–Zwanzig projection operator technique.[37–39] In contrast to focusing only on the dynamics within $\hat{\mathcal{P}}\hat{\rho}$ as in this work, these approaches explicitly treat the interaction between $\hat{\mathcal{P}}\hat{\rho}$ and $\hat{\mathcal{Q}}\hat{\rho}$ to calculate time-dependent memory kernels or rate constants involving both populations and coherences. Therefore, it is natural to conceive of these QMEs as adequate starting points for constructing theories of dissipation under coherent subsystem dynamics. Below, we list some desired requirements for such theories:

- To calculate the dissipation rate into a single bath mode, it must be possible to construct an expression equivalent to Eq. (28) by separating the dynamical evolution of the bath mode from the rest of the system as in Eqs. (29) and (30).
- The consistency between the original QME and the dissipation rate should be rigorously validated, as we did for Eqs. (27) and (35) of Ref. 14 in Appendix A and B therein. It is also straightforward to show that the Hamiltonian employed in this work [Eqs. (1)–(4)] is a specific case of Eqs. (A1)–(A3) of Ref. 14, thereby satisfying the condition for the desired consistency.
- If additional approximations (e.g., Markov approximation) were made for the sake of deriving practical expressions, they need to be checked again for energy conservation and detailed balance (Sec. II C), especially at the steady-state limit $(t \to \infty)$.

IV. CONCLUSIONS

In this paper, we have presented a significant advance in understanding energy dissipation in open quantum systems by introducing a general theoretical framework that complements our previous theory of dissipation pathways in open quantum systems, QME-D, to include off-diagonal subsystem–bath coupling. This generalization is essential for a more realistic treatment of molecular systems where such couplings predominantly affect the quantum dynamics. In particular, we provided a systematic derivation of quantum master equations that describe population transfer and quantify the energy dissipated into individual bath components. Our theoretical formulation is further supported by rigorous proofs of energy conservation and detailed balance, which establish the physical integrity.

The robustness and practical utility of the method were validated through its application to linearly coupled harmonic oscillator baths, which we referred to as MRT-D, as it is consistent with the modified Redfield theory. For quantitative assessment of the accuracy, we tested MRT-D against HEOM-D, a formally exact method for calculating the dissipation. The model Hamiltonians used for the analysis included molecular dimers, spin-boson models, and molecular trimers, with baths described by DL and BO SPDs. We confirmed that, across a significant parameter range, MRT-D demonstrated good to excellent agreement with HEOM-D for both population dynamics and frequency-resolved dissipation spectra. Importantly, MRT-D successfully reproduced key spectral dissipation features, such as vibronic resonances in molecular dimers, site-dependent dissipation, and characteristic peaks in underdamped Brownian oscillator baths. All of these highlight the theory's ability to capture the detailed physics of the dissipation process. The

advantages of MRT-D were particularly evident in molecular trimer simulations, where it resolves dissipation pathways in scenarios where QME-D fails. However, the validation studies of MRT-D also revealed that its accuracy may be reduced in the parameter regimes with strong subsystem–bath coupling, small energy gaps, or highly non-Markovian baths.

We note that, although the simulations presented employ the Condon approximation, our theoretical framework [Eqs. (36) and (37)] can capture non-Condon contributions. This is because the mathematical form of the Hamiltonian in the exciton basis, Eqs. (9) and (10), is unaffected by the addition of any off-diagonal subsystem–bath couplings in the diabatic basis. Non-Condon effects are often important in realistic models of molecular quantum dynamics.[40–43] Applications of our theory to study their consequence in the dissipation pathways will be an interesting direction for future work.

The application of our method is envisioned to be particularly powerful when integrated with sophisticated model Hamiltonians tailored for specific molecular systems. In particular, the method is well-suited to leveraging realistic, highly structured SPDs, whether derived from rigorous QM/MM simulations[2,44–49] or from fitting linearly coupled harmonic bath models to experimental spectroscopic data.[50–57] The approach enables pinpointing the regions within these SPDs that most significantly affect the dynamical evolution of the subsystem. Correlating these influential spectral features with molecular vibrational characteristics, in turn, can offer more comprehensive insights into how vibronic interactions steer non-adiabatic processes. These insights are helpful, for example, in accessing energy dissipation pathways through spectroscopic techniques such as 2D electronic spectroscopy.[58] Ultimately, we envision a broad application of the framework to deepen our understanding of quantum dynamics across a wide range of complex molecular assemblies, including photosynthetic complexes,[1,59,60] artificial excitonic[61–64] and plasmonic systems,[65,66] and molecular or solid-state qubits.[67–69]

ACKNOWLEDGMENTS

C.W.K. was financially supported by the National Research Foundation of Korea (NRF) grants funded by the Ministry of Science and ICT of Korea (Grant Nos. 2022R1F1A1074027 and 2023M3K5A1094813) and the Global Learning and Academic Research Institution for Masters, Ph.D. Students, and Postdocs (LAMP) Program funded by the Ministry of Education of Korea (Grant No. RS-2024-00442775). This material is based upon work supported by the U.S. Department of Energy, Office of Science, Office of Basic Energy Sciences, Quantum Information Science Research in Chemical Sciences, Geosciences, and Biosciences Program under Award No. DE-SC0025334.

AUTHOR DECLARATIONS

Conflict of Interest

The authors have no conflicts to disclose.

Author Contributions

Ignacio Gustin: Conceptualization (equal); Formal analysis (equal); Investigation (equal); Methodology (equal); Project administration (equal); Resources (equal); Software (equal); Validation (equal); Visualization (supporting); Writing – original draft (equal); Writing – review & editing (equal). **Chang Woo Kim**: Conceptualization (equal); Data curation (equal); Formal analysis (equal); Funding acquisition (equal); Investigation (equal); Methodology (equal); Project administration (equal); Resources (equal); Software (equal); Supervision (equal); Validation (equal); Visualization (equal); Writing – original draft (equal); Writing – review & editing (equal). **Ignacio Franco**: Conceptualization (equal); Funding acquisition (equal); Investigation (equal); Methodology (equal); Project administration (equal); Resources (equal); Supervision (equal); Validation (equal); Visualization (equal); Writing – original draft (equal); Writing – review & editing (equal).

DATA AVAILABILITY

The data that support the findings of this study are available within the article.

APPENDIX A: DERIVATION OF EQ. (63)

This appendix presents the detailed procedure for deriving Eq. (63), which are the analytical expressions of the traces in Eqs. (22b) and (22d) under a linearly coupled harmonic oscillator bath. For $\mathrm{Tr}1^j_{\beta\alpha}$ and $\mathrm{Tr}2^j_{\beta\alpha}$, we observe that

$$\begin{aligned}\frac{d\,\mathrm{Tr}0^j_{\beta\alpha}}{dt'} &= -\frac{i}{\hbar}\mathrm{Tr}_j\left[(\hat{u}^j_\alpha)^\dagger(\hat{v}^j_{\beta\beta}-\hat{v}^j_{\alpha\alpha})\hat{u}^j_\beta\hat{r}^j_\alpha\right]\\ &= -\frac{i}{\hbar}\mathrm{Tr}_j\left[(\hat{u}^j_\alpha)^\dagger\hat{u}^j_\beta(\hat{v}^j_{\beta\beta}-\hat{v}^j_{\alpha\alpha})\hat{r}^j_\alpha\right]\end{aligned} \tag{A1}$$

by expanding the bracket in the trace and recognizing the commutativity between the operators. We then plug in the expressions for $\hat{v}^j_{\alpha\alpha}$, $\hat{v}^j_{\beta\beta}$, and $\mathrm{Tr}0^j_{\beta\alpha}$ [Eqs. (58a), (58b), and (59)], and rearrange the resulting equations to yield

$$\mathrm{Tr}_j[(\hat{u}^j_\alpha)^\dagger\hat{y}_j\hat{u}^j_\beta r^j_\alpha] = \mathrm{Tr}_j[(\hat{u}^j_\alpha)^\dagger\hat{u}^j_\beta\hat{y}_j r^j_\alpha] = \left(\frac{d^j_{\beta\beta}-d^j_{\alpha\alpha}}{2}[1+i\dot{f}(\omega_j,t)]\right) \times \mathrm{Tr}0^j_{\beta\alpha}. \tag{A2}$$

We can now insert Eqs. (58c) and (58d) into Eqs. (22b) and (22c), respectively, and use the above results to arrive at Eqs. (63a) and (63b).

For $\mathrm{Tr}3^j_{\beta\alpha}$, we take the time derivative of Eq. (A1) to get

$$\frac{d^2\,\mathrm{Tr}0^j_{\beta\alpha}}{dt'^2} = -\frac{1}{\hbar^2}\mathrm{Tr}_j[(\hat{u}^j_\alpha)^\dagger(\hat{v}^j_{\beta\beta}-\hat{v}^j_{\alpha\alpha})\hat{u}^j_\beta(\hat{v}^j_{\beta\beta}-\hat{v}^j_{\alpha\alpha})\hat{r}^j_\alpha], \tag{A3}$$

from which we can derive

$$\mathrm{Tr}_j[(\hat{u}^j_\alpha)^\dagger\hat{y}_j\hat{u}^j_\beta\hat{y}_j\hat{r}^j_\alpha] = \left(\frac{(d^j_{\beta\beta}-d^j_{\alpha\alpha})^2}{4}[1+i\dot{f}(\omega_j,t)]^2+\frac{\hbar}{2\omega_j^2}\ddot{f}(\omega_j,t)\right) \times \mathrm{Tr}0^j_{\beta\alpha} \tag{A4}$$

with the help of Eq. (A2). Equation (63c) then emerges from Eq. (22d) by taking a similar procedure as we did for $\mathrm{Tr}1^j_{\beta\alpha}$ and $\mathrm{Tr}2^j_{\beta\alpha}$.

APPENDIX B: DISCRETIZATION OF THE BATH SPECTRAL DENSITIES

For the DL SPD [Eq. (81)], our discretization scheme follows Ref. 70, which places the individual bath modes along the frequency axis according to

$$\omega_j = \frac{j^2}{n^2}\omega_{\max}, \quad j = 1, 2, \ldots, n. \tag{B1}$$

Here, n is the total number of discrete modes representing the SPD, and $\omega_{\max}$ is the upper limit of the frequency. This formula results in a denser distribution of modes at lower frequencies, which is appropriate because the reorganization energy density, $J_{\mathrm{DL}}(\omega)/\omega$, is typically larger in this region.

We now define a function $f_{\mathrm{DL}}(\omega)$, which links the discrete and continuous representations of the SPD as

$$\frac{\omega_j^3 d_j^2}{2} = \frac{J_{\mathrm{DL}}(\omega_j)}{f_{\mathrm{DL}}(\omega_j)}. \tag{B2}$$

The explicit form of this function is given by

$$f_{\mathrm{DL}}(\omega) = \frac{n}{2\sqrt{\omega\omega_{\max}}}, \tag{B3}$$

which allows us to obtain the discrete reorganization energy, λ_j, as

$$\lambda_j = \frac{\omega_j^2 d_j^2}{2} = \frac{4\Lambda}{j\pi}\frac{\omega_c\omega_j}{\omega_j^2 + \omega_c^2}. \tag{B4}$$

This value of λ_j is a good approximation for the reorganization energy obtained by integrating $J_{\mathrm{DL}}(\omega)/\omega$ over a frequency segment that corresponds to the jth bath mode, $[(\omega_j + \omega_{j-1})/2, (\omega_j + \omega_{j+1})/2]$,

$$\int_{\text{segment}} \frac{J_{\mathrm{DL}}(\omega)}{\omega} d\omega \approx \frac{J_{\mathrm{DL}}(\omega_j)}{\omega_j}\Delta\omega_j = \frac{4\Lambda}{j\pi}\frac{\omega_c\omega_j}{\omega_j^2 + \omega_c^2}. \tag{B5}$$

Here, $\Delta\omega_j$ is the length of the segment.

For the BO SPD [Eq. (82)] with the characteristic frequency ω_0 and damping parameter γ, we set $\omega_{\max} > \omega_0$ and calculate the frequency Ω that maximizes the reorganization energy density $J_{\mathrm{BO}}(\omega)/\omega$,

$$\Omega = \sqrt{\max\left[0, \omega_0^2 - 2\gamma^2\right]}. \tag{B6}$$

If $\Omega = 0$, we can follow the discretization strategy similar to that for the DL SPD [Eqs. (B1)–(B3)], by substituting $J_{\mathrm{DL}}(\omega)$ with $J_{\mathrm{BO}}(\omega)$. Otherwise, the frequency domain is split into two windows $[0, \Omega)$ and $(\Omega, \omega_{\max}]$, each of which is represented by $n/2$ bath modes using separate discretization schemes. For the $[0, \Omega)$ window, we have

$$\begin{aligned} \omega_{1,j} &= \left[1 - \left(1 - \frac{2j}{n}\right)^2\right]\Omega, \\ f_{\mathrm{BO1}}(\omega) &= \frac{n}{4\sqrt{(\Omega - \omega)\Omega}}, \quad j = 1, 2, \ldots, \frac{n}{2} - 1, \end{aligned} \tag{B7}$$

and for the $(\Omega, \omega_{\max}]$ window,

$$\begin{aligned} \omega_{2,j} &= \Omega + \frac{4j^2}{n^2}(\omega_{\max} - \Omega), \\ f_{\mathrm{BO2}}(\omega) &= \frac{n}{4\sqrt{(\omega - \Omega)(\omega_{\max} - \Omega)}}, \quad j = 1, 2, \ldots, \frac{n}{2}. \end{aligned} \tag{B8}$$

Equations (B7) and (B8) do not include a bath mode placed exactly at $\omega = \Omega$, where both $f_{\mathrm{BO1}}(\omega)$ and $f_{\mathrm{BO2}}(\omega)$ diverge. Nevertheless, we can resolve this issue by assigning this mode a specific reorganization energy $\lambda_{\omega=\Omega}$, which is determined to match the integral of $J_{\mathrm{BO}}(\omega)/\omega$ over the frequency interval near $\omega = \Omega$ that is not yet covered by the bath modes in Eqs. (B7) and (B8). The result is

$$\lambda_{\omega=\Omega} = \frac{2\Lambda}{\pi n^2}\frac{\omega_{\max}\omega_0^2}{\gamma(\omega_0^2 - \gamma^2)}. \tag{B9}$$

As a result, similar to the discretization of DL SPD, the bath modes become more concentrated in the region around $\omega = \Omega$, which makes a dominant contribution to the overall subsystem–bath coupling.

REFERENCES

[1] T. Mirkovic, E. E. Ostroumov, J. M. Anna, R. van Grondelle, and G. D. Scholes, "Light absorption and energy transfer in the antenna complexes of photosynthetic organisms," Chem. Rev. **117**, 249–293 (2017).

[2] S. J. Jang and B. Mennucci, "Delocalized excitons in natural light-harvesting complexes," Rev. Mod. Phys. **90**, 035003 (2018).

[3] J. Cao, R. J. Cogdell, D. F. Coker, H.-G. Duan, J. Hauer, U. Kleinekathöfer, T. L. C. Jansen, T. Mančal, R. J. D. Miller, J. P. Ogilvie, V. I. Prokhorenko, T. Renger, H.-S. Tan, R. Tempelaar, M. Thorwart, E. Thyrhaug, S. Westenhoff, and D. Zigmantas, "Quantum biology revisited," Sci. Adv. **6**, eaaz4888 (2020).

[4] D. Kienzler, H.-Y. Lo, B. Keitch, L. de Clercq, F. Leupold, F. Lindenfelser, M. Marinelli, V. Negnevitsky, and J. P. Home, "Quantum harmonic oscillator state synthesis by reservoir engineering," Science **347**, 53–56 (2014).

[5] J. A. Campos-Gonzalez-Angulo, R. F. Ribeiro, and J. Yuen-Zhou, "Resonant catalysis of thermally activated chemical reactions with vibrational polaritons," Nat. Commun. **10**, 4685 (2019).

[6] K. Ng, M. Webster, W. P. Carbery, N. Visaveliya, P. Gaikwad, S. J. Jang, I. Kretzschmar, and D. M. Eisele, "Frenkel excitons in heat-stressed supramolecular nanocomposites enabled by tunable cage-like scaffolding," Nat. Chem. **12**, 1157–1164 (2020).

[7] S. M. Hart, W. J. Chen, J. L. Banal, W. P. Bricker, A. Dodin, L. Markova, Y. Vyborna, A. P. Willard, R. Häner, M. Bathe, and G. S. Schlau-Cohen, "Engineering couplings for exciton transport using synthetic DNA scaffolds," Chem **7**, 752–773 (2021).

[8] W. Hu, I. Gustin, T. D. Krauss, and I. Franco, "Tuning and enhancing quantum coherence time scales in molecules via light-matter hybridization," J. Phys. Chem. Lett. **13**, 11503–11511 (2022).

[9] M. H. Beck, A. Jäckle, G. A. Worth, and H.-D. Meyer, "The multiconfiguration time-dependent Hartree (MCTDH) method: A highly efficient algorithm for propagating wavepackets," Phys. Rep. **324**, 1–105 (2000).

[10] S. Kundu, R. Dani, and N. Makri, "Tight inner ring architecture and quantum motion of nuclei enable efficient energy transfer in bacterial light harvesting," Sci. Adv. **8**, eadd0023 (2022).

[11] A. Strathearn, P. Kirton, D. Kilda, J. Keeling, and B. W. Lovett, "Efficient non-Markovian quantum dynamics using time-evolving matrix product operators," Nat. Commun. **9**, 3322 (2018).

[12] L. Varvelo, J. K. Lynd, and D. I. G. Bennett, "Formally exact simulations of mesoscale exciton dynamics in molecular materials," Chem. Sci. **12**, 9704–9711 (2021).

[13]A. Bose and P. L. Walters, "A multisite decomposition of the tensor network path integrals," J. Chem. Phys. **156**, 024101 (2022).
[14]C. W. Kim and I. Franco, "General framework for quantifying dissipation pathways in open quantum systems. I. Theoretical formulation," J. Chem. Phys. **160**, 214111 (2024).
[15]S. Nakajima, "On quantum theory of transport phenomena: Steady diffusion," Prog. Theor. Phys. **20**, 948–959 (1958).
[16]R. Zwanzig, "Ensemble method in the theory of irreversibility," J. Chem. Phys. **33**, 1338–1341 (1960).
[17]C. W. Kim and I. Franco, "Theory of dissipation pathways in open quantum systems," J. Chem. Phys. **154**, 084109 (2021).
[18]I. Gustin, C. W. Kim, and I. Franco, "Dissipation pathways in a photosynthetic complex," J. Phys. Chem. Lett. **16**, 13093–13101 (2025).
[19]C. W. Kim and I. Franco, "General framework for quantifying dissipation pathways in open quantum systems. II. Numerical validation and the role of non-Markovianity," J. Chem. Phys. **160**, 214112 (2024).
[20]M. Yang and G. R. Fleming, "Influence of phonons on exciton transfer dynamics: Comparison of the Redfield, Förster, and modified Redfield equations," Chem. Phys. **275**, 355–372 (2002).
[21]E. Mulvihill and E. Geva, "A road map to various pathways for calculating the memory kernel of the generalized quantum master equation," J. Phys. Chem. B **125**, 9834–9852 (2021).
[22]J. Sung and R. J. Silbey, "Four wave mixing spectroscopy for a multilevel system," J. Chem. Phys. **115**, 9266–9287 (2001).
[23]S. Mukamel, "Nonimpact unified theory of four-wave mixing and two-photon processes," Phys. Rev. A **28**, 3480–3492 (1983).
[24]S.-J. Jang, "Multistep quantum master equation theory for response functions in four wave mixing electronic spectroscopy of multichromophoric macromolecules," Bull. Korean Chem. Soc. **33**, 997–1008 (2012).
[25]S. Jang, Y. Jung, and R. J. Silbey, "Nonequilibrium generalization of Förster–Dexter theory for excitation energy transfer," Chem. Phys. **275**, 319–332 (2002).
[26]W. M. Zhang, T. Meier, V. Chernyak, and S. Mukamel, "Exciton-migration and three-pulse femtosecond optical spectroscopies of photosynthetic antenna complexes," J. Chem. Phys. **108**, 7763–7774 (1998).
[27]E. U. Condon, "Nuclear motions associated with electron transitions in diatomic molecules," Phys. Rev. **32**, 858–872 (1928).
[28]M. Tanaka and Y. Tanimura, "Multistate electron transfer dynamics in the condensed phase: Exact calculations from the reduced hierarchy equations of motion approach," J. Chem. Phys. **132**, 214502 (2010).
[29]A. Ishizaki and Y. Tanimura, "Modeling vibrational dephasing and energy relaxation of intramolecular anharmonic modes for multidimensional infrared spectroscopies," J. Chem. Phys. **125**, 084501 (2006).
[30]Y. Tanimura, "Numerically exact approach to open quantum dynamics: The hierarchical equations of motion (HEOM)," J. Chem. Phys. **153**, 020901 (2020).
[31]C. W. Kim, "Extracting bath information from open-quantum-system dynamics with the hierarchical equations-of-motion method," Phys. Rev. A **106**, 042223 (2022).
[32]T. C. Berkelbach, T. E. Markland, and D. R. Reichman, "Reduced density matrix hybrid approach: Application to electronic energy transfer," J. Chem. Phys. **136**, 084104 (2012).
[33]A. Montoya-Castillo, T. C. Berkelbach, and D. R. Reichman, "Extending the applicability of redfield theories into highly non-Markovian regimes," J. Chem. Phys. **143**, 194108 (2015).
[34]T. P. Fay, "A simple improved low temperature correction for the hierarchical equations of motion," J. Chem. Phys. **157**, 054108 (2022).
[35]E. Fehlberg, *Low-Order Classical Runge-Kutta Formulas With Stepsize Control and Their Application to Some Heat Transfer Problems* (National Aeronautics and Space Administration, 1969), Vol. 315.
[36]T. Ikeda and G. D. Scholes, "Generalization of the hierarchical equations of motion theory for efficient calculations with arbitrary correlation functions," J. Chem. Phys. **152**, 204101 (2020).
[37]A. Trushechkin, "Calculation of coherences in Förster and modified Redfield theories of excitation energy transfer," J. Chem. Phys. **151**, 074101 (2019).
[38]Y. Lai and E. Geva, "On simulating the dynamics of electronic populations and coherences via quantum master equations based on treating off-diagonal electronic coupling terms as a small perturbation," J. Chem. Phys. **155**, 204101 (2021).
[39]A. Kimura, "Extended perturbative approach including Redfield and Förster limits for qualitative analysis of exciton dynamics in any photosynthetic light harvesting and reaction center," J. Chem. Phys. **161**, 124102 (2024).
[40]S. S. Skourtis, I. A. Balabin, T. Kawatsu, and D. N. Beratan, "Protein dynamics and electron transfer: Electronic decoherence and non-Condon effects," Proc. Natl. Acad. Sci. U. S. A. **102**, 3552–3557 (2005).
[41]H. Nishioka, A. Kimura, T. Yamato, T. Kawatsu, and T. Kakitani, "Interference, fluctuation, and alternation of electron tunneling in protein media. II. Non-Condon theory for the energy gap dependence of electron transfer rate," J. Phys. Chem. B **109**, 15621–15635 (2005).
[42]S. Jang and M. D. Newton, "Theory of torsional non-Condon electron transfer: A generalized spin-boson Hamiltonian and its nonadiabatic limit solution," J. Chem. Phys. **122**, 024501 (2005).
[43]S. Jang, "Generalization of the Förster resonance energy transfer theory for quantum mechanical modulation of the donor-acceptor coupling," J. Chem. Phys. **127**, 174710 (2007).
[44]S. Maity, V. Daskalakis, M. Elstner, and U. Kleinekathöfer, "Multiscale QM/MM molecular dynamics simulations of the trimeric major light-harvesting complex II," Phys. Chem. Chem. Phys. **23**, 7407–7417 (2021).
[45]C. W. Kim, B. Choi, and Y. M. Rhee, "Excited state energy fluctuations in the Fenna–Matthews–Olson complex from molecular dynamics simulations with interpolated chromophore potentials," Phys. Chem. Chem. Phys. **20**, 3310–3319 (2018).
[46]E. Cignoni, V. Slama, L. Cupellini, and B. Mennucci, "The atomistic modeling of light-harvesting complexes from the physical models to the computational protocol," J. Chem. Phys. **156**, 120901 (2022).
[47]M. K. Lee and D. F. Coker, "Modeling electronic-nuclear interactions for excitation energy transfer processes in light-harvesting complexes," J. Phys. Chem. Lett. **7**, 3171–3178 (2016).
[48]A. Kell, X. Feng, M. Reppert, and R. Jankowiak, "On the shape of the phonon spectral density in photosynthetic complexes," J. Phys. Chem. B **117**, 7317–7323 (2013).
[49]M. S. Chen, Y. Mao, A. Snider, P. Gupta, A. Montoya-Castillo, T. J. Zuehlsdorff, C. M. Isborn, and T. E. Markland, "Elucidating the role of hydrogen bonding in the optical spectroscopy of the solvated green fluorescent protein chromophore: Using machine learning to establish the importance of high-level electronic structure," J. Phys. Chem. Lett. **14**, 6610–6619 (2023).
[50]M. Rätsep and A. Freiberg, "Electron–phonon and vibronic couplings in the FMO bacteriochlorophyll *a* antenna complex studied by difference fluorescence line narrowing," J. Lumin. **127**, 251–259 (2007).
[51]M. Rätsep, J. Pieper, K.-D. Irrgang, and A. Freiberg, "Excitation wavelength-dependent electron- phonon and electron- vibrational coupling in the CP29 antenna complex of green plants," J. Phys. Chem. B **112**, 110–118 (2008).
[52]J. Pieper, M. Rätsep, I. Trostmann, F.-J. Schmitt, C. Theiss, H. Paulsen, H. Eichler, A. Freiberg, and G. Renger, "Excitonic energy level structure and pigment-protein interactions in the recombinant water-soluble chlorophyll protein. II. Spectral hole-burning experiments," J. Phys. Chem. B **115**, 4053–4065 (2011).
[53]I. Gustin, X. Chen, and I. Franco, "Decoherence dynamics in molecular qubits: Exponential, Gaussian and beyond," J. Chem. Phys. **162**, 064106 (2025).
[54]J. Pieper, M. Rätsep, K.-D. Irrgang, and A. Freiberg, "Chromophore-chromophore and chromophore-protein interactions in monomeric light-harvesting complex II of green plants studied by spectral hole burning and fluorescence line narrowing," J. Phys. Chem. B **113**, 10870–10880 (2009).
[55]A. Freiberg, M. Rätsep, K. Timpmann, and G. Trinkunas, "Excitonic polarons in quasi-one-dimensional LH1 and LH2 bacteriochlorophyll *a* antenna aggregates from photosynthetic bacteria: A wavelength-dependent selective spectroscopy study," Chem. Phys. **357**, 102–112 (2009).

[56]G. Gryliuk, M. Rätsep, S. Hildebrandt, K.-D. Irrgang, H.-J. Eckert, and J. Pieper, "Excitation energy transfer and electron-vibrational coupling in phycobiliproteins of the cyanobacterium *Acaryochloris marina* investigated by site-selective spectroscopy," Biochim. Biophys. Acta, Bioenerg. **1837**, 1490–1499 (2014).
[57]I. Gustin, C. W. Kim, D. W. McCamant, and I. Franco, "Mapping electronic decoherence pathways in molecules," Proc. Natl. Acad. Sci. U. S. A. **120**, e2309987120 (2023).
[58]R. de Wit, J. Keeling, B. W. Lovett, and A. W. Chin, "Extracting coupling-mode spectral densities with two-dimensional electronic spectroscopy," J. Phys. Chem. Lett. **16**, 6594–6601 (2025).
[59]S. M. Blau, D. I. G. Bennett, C. Kreisbeck, G. D. Scholes, and A. Aspuru-Guzik, "Local protein solvation drives direct down-conversion in phycobiliprotein PC645 via incoherent vibronic transport," Proc. Natl. Acad. Sci. U. S. A. **115**, E3342–E3350 (2018).
[60]J. M. Womick and A. M. Moran, "Vibronic enhancement of exciton sizes and energy transport in photosynthetic complexes," J. Phys. Chem. B **115**, 1347–1356 (2011).
[61]F. Häse, L. M. Roch, P. Friederich, and A. Aspuru-Guzik, "Designing and understanding light-harvesting devices with machine learning," Nat. Commun. **11**, 4587 (2020).
[62]L. Bolzonello, F. Fassioli, and E. Collini, "Correlated fluctuations and intraband dynamics of J-aggregates revealed by combination of 2DES schemes," J. Phys. Chem. Lett. **7**, 4996–5001 (2016).
[63]L. Yang and S. J. Jang, "Theoretical investigation of non-Förster exciton transfer mechanisms in perylene diimide donor, phenylene bridge, and terrylene diimide acceptor systems," J. Chem. Phys. **153**, 144305 (2020).
[64]A. L. Bialas and F. C. Spano, "A Holstein–Peierls approach to excimer spectra: The evolution from vibronically structured to unstructured emission," J. Phys. Chem. C **126**, 4067–4081 (2022).
[65]L.-Y. Hsu, W. Ding, and G. C. Schatz, "Plasmon-coupled resonance energy transfer," J. Phys. Chem. Lett. **8**, 2357–2367 (2017).
[66]P. Bai, S. ter Huurne, E. van Heijst, S. Murai, and J. Gómez Rivas, "Evolutionary optimization of light-matter coupling in open plasmonic cavities," J. Chem. Phys. **154**, 134110 (2021).
[67]J. M. Gertler, B. Baker, J. Li, S. Shirol, J. Koch, and C. Wang, "Protecting a bosonic qubit with autonomous quantum error correction," Nature **590**, 243–248 (2021).
[68]P. M. Harrington, E. J. Mueller, and K. W. Murch, "Engineered dissipation for quantum information science," Nat. Rev. Phys. **4**, 660–671 (2022).
[69]A. Chiesa, A. Privitera, E. Macaluso, M. Mannini, R. Bittl, R. Naaman, M. R. Wasielewski, R. Sessoli, and S. Carretta, "Chirality-induced spin selectivity: An enabling technology for quantum applications," Adv. Mater. **35**, 2300472 (2023).
[70]H. Wang, X. Song, D. Chandler, and W. H. Miller, "Semiclassical study of electronically nonadiabatic dynamics in the condensed-phase: Spin-boson problem with Debye spectral density," J. Chem. Phys. **110**, 4828–4840 (1999).